Evidence of phyllosilicates in Wooly Patch, an altered rock encountered at West Spur, Columbia Hills, by the Spirit rover in Gusev crater, Mars

Alian Wang,[1] Randy L. Korotev,[1] Bradley L. Jolliff,[1] Larry A. Haskin,[1,2] Larry Crumpler,[3] William H. Farrand,[4] Ken E. Herkenhoff,[5] Paulo de Souza Jr.,[6] Alastair G. Kusack,[7] Joel A. Hurowitz,[8] and Nicholas J. Tosca[8]

Received 22 June 2005; revised 31 October 2005; accepted 7 November 2005; published 15 February 2006.

[1] On its traverse to Columbia Hills, the Mars Exploration Rover Spirit investigated an outcrop designated ''Wooly Patch'' that exhibited morphological, mineralogical, and geochemical characteristics at the extreme ends of ranges observed among rocks studied at West Spur, a westward projecting salient near the foot of the Columbia Hills, Gusev crater. The major-element composition and Fe-mineralogy, as determined by the Alpha-Particle X-ray Spectrometer and Mössbauer Spectrometer, are inconsistent with any reasonable assemblage of basaltic minerals in that there is an excess of Si and Al. The combined data are best explained by the presence of 14–17% phyllosilicate minerals. Phyllosilicates that account for the composition and cation ratios include members of the kaolinite, serpentine, chlorite, and septechlorite groups. The potential existence of kaolinite-type Al-rich phyllosilicates within the Wooly Patch outcrop suggests a mildly acidic environment (pH 4–6) in the past and an open hydrologic system with good drainage conditions in the environment where these rocks were altered.

Citation: Wang, A., et al. (2006), Evidence of phyllosilicates in Wooly Patch, an altered rock encountered at West Spur, Columbia Hills, by the Spirit rover in Gusev crater, Mars, *J. Geophys. Res.*, *111*, E02S16, doi:10.1029/2005JE002516.

1. Introduction

[2] Most of the rocks analyzed during the primary mission (through Sol 90) of Spirit (Mars Exploration Rover mission 2004–2005) are either impact ejecta from Bonneville crater (~200 m diameter, ~ 300 m from the landing site) or derived from small impacts into the Gusev plains basalts [*Squyres et al.*, 2004]. The interiors of rocks in this region (Adirondack, Humphrey, Mazatzal) have characteristics of olivine-rich basalt [*McSween et al.*, 2004, 2006]. A high oxidation state (evidenced by the presence of hematite [*Morris et al.*, 2004]) and high S, Cl, and Br concentrations [*Gellert et al.*, 2004] characterize the multilayered coatings of the light-toned rock Mazatzal, suggesting postcrystallization aqueous alteration [*Haskin et al.*, 2005].

[3] During the extended mission (sols 91–156), Spirit traveled about 2.3 km across the plains between Bonneville crater and the Columbia Hills [*Crumpler et al.*, 2005]. Plains basalts are the only rock type identified along the traverse, as determined by in situ chemistry, Fe-mineralogy, and surface morphology measurements on two rocks (Route 66 and Joshua) using the Alpha-Particle X-ray Spectrometer (APXS), Mössbauer Spectrometer (MB) and Microscopic Imager (MI) [*Herkenhoff et al.*, 2003; *Klingelhöfer et al.*, 2003; *Rieder et al.*, 2003] or by remote-sensing geomorphology and spectroscopic measurements on many other rocks using the Panoramic Camera (Pancam) and the Miniature Thermal Emission Spectrometer (Mini-TES) [*Bell et al.*, 2003; *Christensen et al.*, 2003]. Sulfate deposition, however, in the regolith within the two deep trenches in the plains (the Big Hole and The Boroughs trenches) is indicated by compositional data; a low degree of alteration of silicate minerals and an increase of oxidation state were also observed [*Haskin et al.*, 2005; *Wang et al.*, 2005b; *Wang et al.*, 2006].

[4] The investigation by Spirit on the Columbia Hills started at the first rock target ''Pot of Gold'' at the foot of West Spur, a westward projecting salient near the foot of Husband Hill. The Athena science team named this rock after the Irish ''leprechaun'' legend because this was the first rock to display the morphological signature of weathering/alteration [*Arvidson et al.*, 2006, Figure 13; *Squyres et al.*, 2006] after the long drive of Spirit from the landing site across the plains to the foot of the Columbia Hills. Wooly Patch was the second rock target on West Spur investigated

[1]Department of Earth and Planetary Sciences and McDonnell Center for Space Science, Washington University in St. Louis, St. Louis, Missouri, USA.
[2]Deceased 24 March 2005.
[3]New Mexico Museum of Natural History and Science, Albuquerque, New Mexico, USA.
[4]Space Science Institute, Boulder, Colorado, USA.
[5]U.S. Geological Survey, Flagstaff, Arizona, USA.
[6]Companhia Vale do Rio Doce, Rio de Janeiro, Brazil.
[7]Honeybee Robotics, New York, New York, USA.
[8]Department of Geosciences, State University of New York, Stony Brook, New York, USA.

0148-0227/06/2005JE002516$09.00

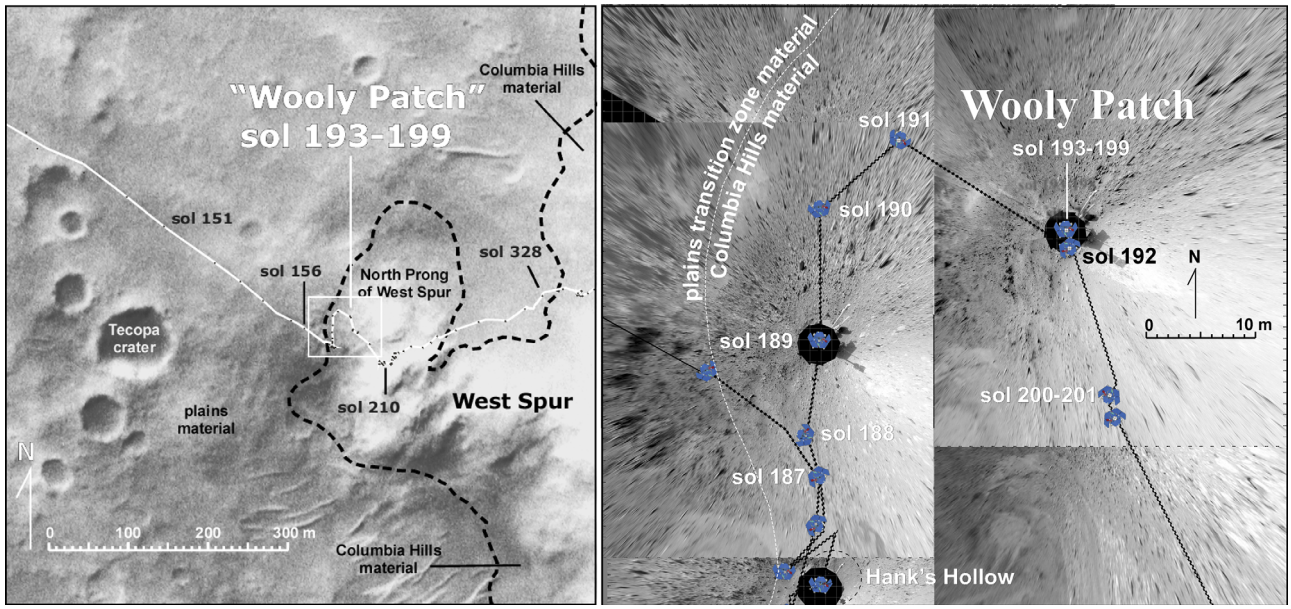

Figure 1. Wooly Patch is located near the northern bend in the initial ascending traverse on the West Spur approximately 35 m from the contact (dashed line) between the plains basalt and older Columbia Hills materials. Enlarged square shows the details of the Spirit travel route near Wooly Patch with a base map as background. The base map is a mosaic of vertically projected Navcam panoramas from sites 69, 72, 76, and 77.

using the full Athena science instrument payload [*Squyres et al.*, 2003]. Prehistoric mammals were the naming theme for this outcrop. The Wooly Patch investigation lasted 9 sols (sols 192–200) [*Wang et al.*, 2005a].

[5] Spirit made a total of eight rock investigations at West Spur, and seven rock investigations on Husband Hill through sol 475 [*Arvidson et al.*, 2006; *Ming et al.*, 2006]. This paper presents the results and analyses only for the Wooly Patch outcrop. Compositions of three plains basalts, four other West Spur rocks, and two rocks on Husband Hill (through sol 357) are used for comparison. Among the APXS data, only those from the rock interiors after abrasion by the RAT (rock abrasion tool) [*Gorevan et al.*, 2003] are used in this paper.

2. Wooly Patch Investigations

2.1. Regional Setting

[6] The Wooly Patch outcrop is located on a northern prong of the West Spur (Figure 1). The Columbia Hills is actually composed of several rounded hills rising about 120 m above the basaltic plains of the Gusev crater floor. On the basis of embayment relationships, the Columbia Hills predate the plains. The relative age of the hills with respect to the plains in terms of cratering chronology are undetermined, but the hills could represent older materials dating from a time in Martian geologic history significantly earlier than the plains emplacement [*Arvidson et al.*, 2006; *Squyres et al.*, 2006].

[7] The Wooly Patch outcrop is located 4.5 m above the contact between the plains and the hills (sol 156) (Figure 2, based on bundle-adjusted data of *Li et al.* [2006]) on a west facing apron descending from the crest of the local relief. Immediately east of the outcrop the surface slopes steeply upward to a ridge littered with rocky materials that appear to characterize the upper surfaces of the West Spur in general.

2.2. Outcrop Description

[8] Compared with surrounding areas on the flanks of the West Spur, the Wooly Patch outcrop is locally distinctive; it appears from a distance (sol 190) to be an area of more integrated, lighter-toned rock mass than the surrounding loose materials and clasts (float). The float materials lie on a broader apron of loose material descending from the local crest of the West Spur (Figure 3) immediately to the east. Another distinctive, darker rock mass, "Viera Cairn," lies within a meter to the east of Wooly Patch (Figure 3). An initial approach to the outcrop on sol 192 placed Spirit on

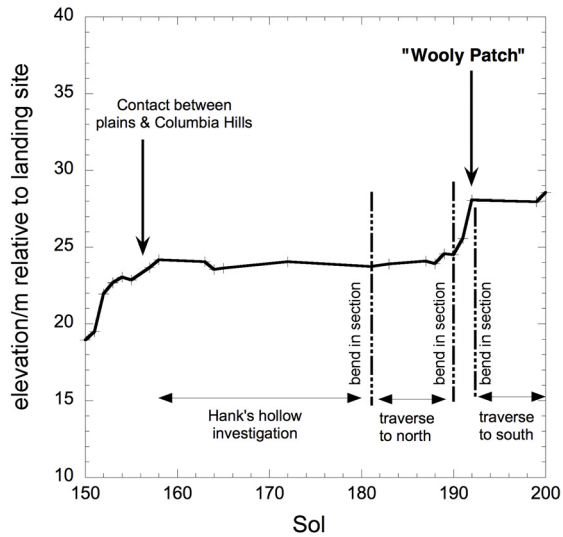

Figure 2. Elevation of Wooly Patch from rover tracking data [*Arvidson et al.*, 2006; *Li et al.*, 2006].

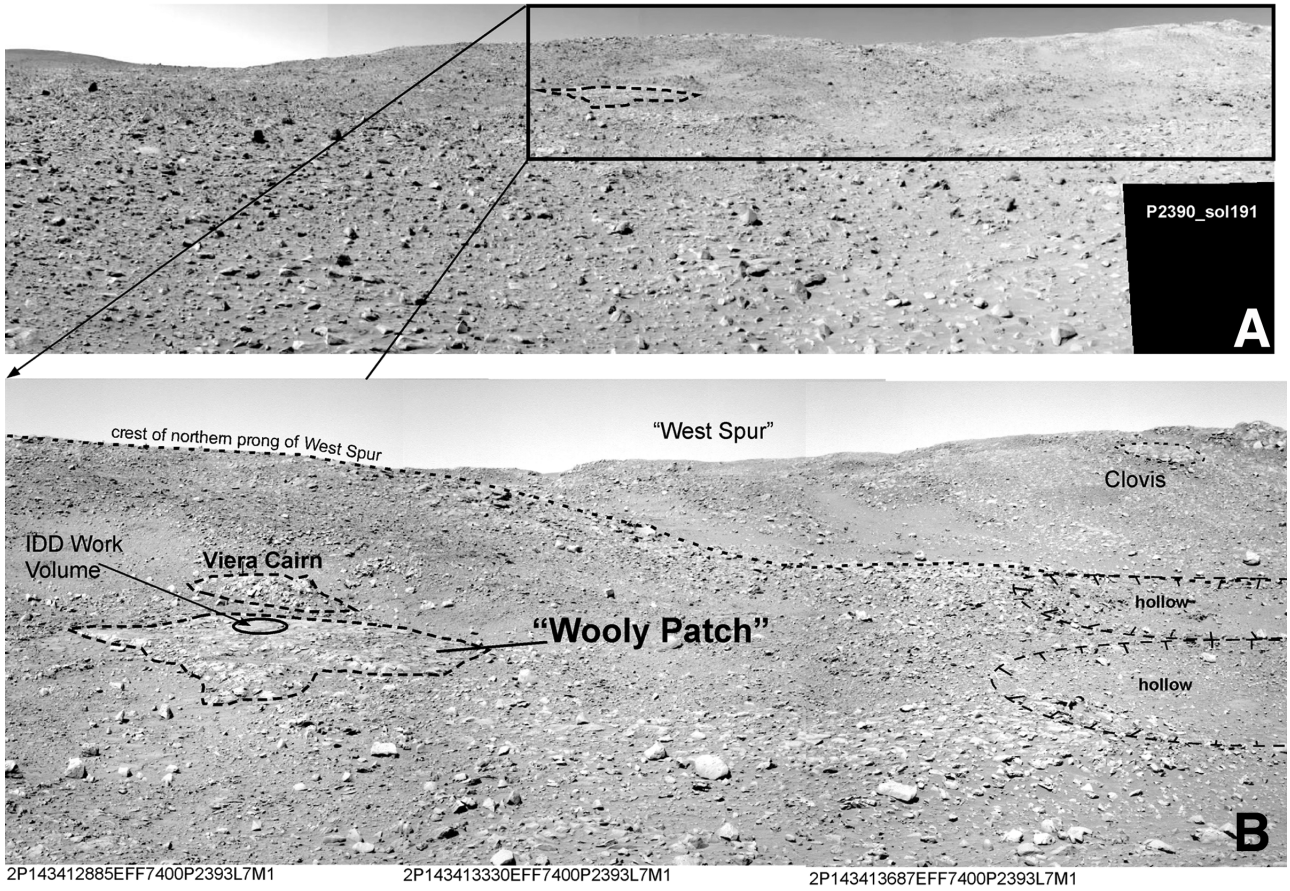

Figure 3. Pancam mosaics acquired on sol 190–191, site 73–74, in the direction of Wooly Patch. This outcrop lies at the foot of a slope ascending to the crest of a local ridge. Viera Cairn is a group of dark-toned rocks lying within a meter to the east of Wooly Patch. Clovis is a highly altered light-toned outcrop farther south along the north face of the West Spur that can be seen in the upper right corner.

the eastern end of Wooly Patch, facing westward (away from Viera Cairn) (see outcrop orientation in Figure 4a). From this location a suitable area for grinding using the RAT (Figure 4d) was selected, which required repositioning of Spirit on sol 193 to a more southerly-facing location in which the front wheels were perched on the outcrop with a northerly tilt of the rover deck (see outcrop orientation in Figure 4b).

[9] Mapping of the Wooly Patch outcrop from both the sol 192 and sol 193 positions in Hazcam and Pancam images show that the outcrop is broadly flat-lying with a slight convex form, that is, it is high in the middle and slopes to the surroundings where the outcrop surface appears to become covered with loose fines. The part of the outcrop with the largest surface area uninterrupted by fractures lies near the crest of the outcrop. Irregular fractures with maximum spacing of several tens of centimeters trace across the central part of the outcrop increasing in density outward where the outcrop appears less integrated.

[10] Hazcam (Figures 4a and 4c) and Pancam (Figures 4d and 4e) images show that where the fractures or joints intercept the outcrop surface the fractures are distinguished by raised margins (Figures 4c and 4e). These raised margins are interpreted to be the result of differential erosion of the outcrop face in which the raised margins reflect relatively more indurated outcrop material adjacent to the fractures, either because the fracture margins have been preferentially "hardened" or because the areas away from fractures have been preferentially "softened."

[11] The megascopic fracture characteristics of the outcrop in which fracture boundaries are raised relative to the surroundings imply relatively greater hardness and resistance to erosion than the surroundings. More indurated areas adjacent to fractures can arise from fluid-activated alteration of the original mineral grains or from initial changes in the grain boundaries that develop at the time of fracture formation. In the case of alteration, similar morphology in weathered outcrops is common on Earth where mineral interstices in areas immediately adjacent to the fluid are strongly cemented or dissolved by materials carried in solution along fractures through which fluid flowed ("solution hardening") [*Robinson and Williams*, 1995]. The process can either increase or decrease the relative hardness of the rock along the fracture walls depending on the timescale over which fluids are available for chemical processes to operate. In areas that have experienced substantial fluid movement in the subsurface, indurated fracture margins occur commonly where the mineral interstices in areas immediately adjacent to the fractures are strongly cemented by materials carried in solution. Alternatively, highly fractured and porous rock masses can become saturated, but drain and dry out along fractures more frequently than the interior rock mass farther removed from fractures. In this case, the areas near fractures

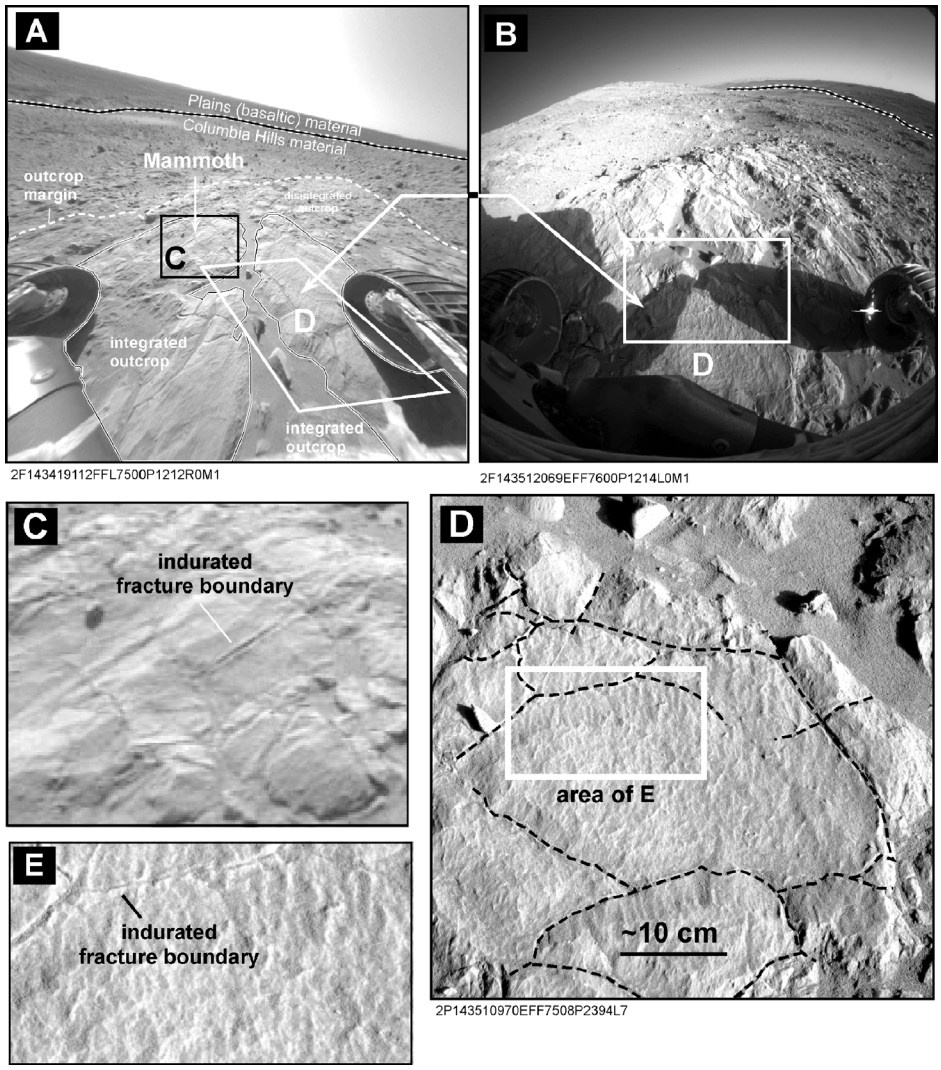

Figure 4. (a) Northwestward directed linearized Hazcam (2F143419112FFL7500P1212R0M1) view across Wooly Patch outcrop on sol 191, site 75 prior to repositioning to orientation shown in Figure 4b, sol 192, site 76. Dashed line indicates the extent of Wooly Patch outcrop material. Solid lines enclose areas of continuous outcrop. (b) Southward directed Hazcam (2F143512069EFF7600P1214L0M1) view on sol 192, site 76 following repositioning of rover for in situ studies of area in Figure 4d. The view to the south beyond the outcrop includes the West Spur on the left and southern rim of Gusev crater on the right horizon. Dashed line marks contact between plains basaltic materials on the right and the Columbia Hills materials. (c) Area indicated in Figure 4a showing fractures within the main mass of the Wooly Patch outcrop distinguished by raised margins. (d) Pancam image (2P143510970EFF7508P2394L7) of outcrop surface prior to RAT abrasions. (e) As in area in Figure 4d, fractures are distinguished by raised margins implying that the fracture walls are relatively indurated relative to the surrounding rock mass.

experience relatively shorter periods of fluid interaction and correspondingly less chemical alteration, and they represent the original grain cohesion. Indurated fracture boundaries might form at the time of fracture formation if a process similar to shock metamorphism occurs, as might happen during propagation of shock through a rock mass during a local impact. This would imply that the induration is a result of local grain boundary melting or fusing, or a similar process operating along planar pathways through the rock mass.

[12] Although the chemical composition of the Wooly Patch outcrop differs from that of Clovis (a nearby outcrop farther south along the north face of the West Spur that can be seen in the upper right corner of Figure 3b), these two outcrops on West Spur bear morphological similarities, including large slab-like character, absence of visible layering, generally light-toned appearance, and occurrence slightly below the cap rock defining the crest of the West Spur. The latter suggests that both outcrops are slumps of either the cap rock material or a layer lying immediately beneath the cap rock materials. However, considering the size of Wooly Patch (2–2.5 m across) and the apparent fragility based on the throughgoing fractures, the displacement, if it occurred, was geologically slow in which the

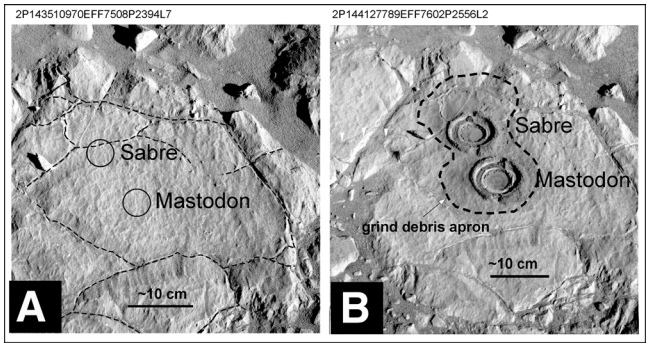

Figure 5. Pancam images of the Wooly Patch outcrop surface (a) before and (b) after RAT abrasions. Target "Sabre" is located adjacent to a prominent fracture (see Figures 4d and 4e). Target "Mastodon" is located in the center of the outcrop, far removed from fractures.

outcrop was gradually let down by undermining of the slopes of the West Spur. A similar process could account also for the slab-like character of the Clovis outcrop.

2.3. Measurements Using the Athena Instrument Payload

[13] Pancam multispectral images were taken before the final approach of Spirit to Wooly Patch, which placed the rock into the work volume of the Instrument Deployment Device (IDD, i.e., robotic arm). Three areas on Wooly Patch were targeted for detailed in situ study; these were named Mammoth, Sabre, and Mastodon (Figures 4a and 5). The first target, Mammoth, is in a part of the outcrop showing multiple fractures and veins cutting through the rock (Figures 4a and 4c). A 2 × 1 Microscopic Imager (MI) mosaic (Figure 6a) and a short-integration Mössbauer spectrum (2.5 hrs) were obtained. Two other targets, Sabre and Mastodon, were selected from a flat and smooth portion of Wooly Patch, after repositioning the rover on sol 193 (Figures 4b, 4d, and 5a). Sabre is located near a narrow vein and Mastodon is away from any apparent veins or fractures. Two RAT grinding operations were performed on Sabre and Mastodon, which produced a hole of 5.17 mm depth at Sabre and a hole of 4.02 mm depth at Mastodon. MI mosaics were taken at both targets prior to grinding (Figures 6b and 6c) and after grinding (Figures 7a and 7b). Mössbauer and alpha particle X-ray fluorescence spectra were obtained on the undisturbed surface of Sabre and on abraded Sabre and abraded Mastodon. After finishing these in situ measurements, a second Pancam multispectral imaging observation and a Mini-TES observation were taken following a ~0.85 m drive back from Wooly Patch. These two observations cover the two RAT-abraded holes and portions of the undisturbed surface on Wooly Patch (Figure 8). More details on the operations and measure-

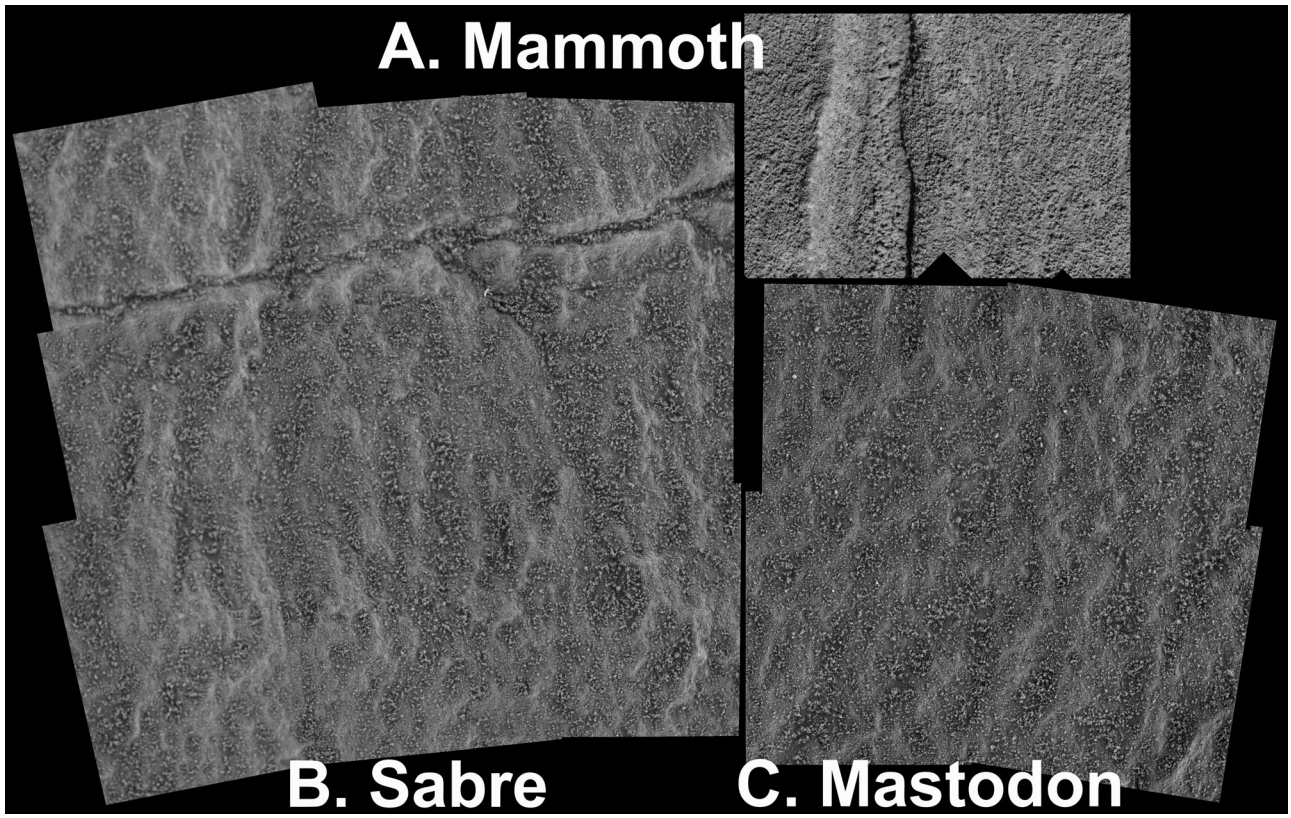

Figure 6. Microscopic image mosaics of as-is undisturbed surfaces (field of view of each frame is ~32 mm, ~30 micrometer/pixel): (a) Target Mammoth, taken on sol 193. Area shown is ~42 mm high; illumination is from the upper right. (b) Target Sabre, taken on sol 194. Area shown is ~89 mm high; target was fully shadowed when images were acquired. (c) Target Mastodon, taken on sol 197. Area shown is ~63 mm across; target was fully shadowed when images were acquired.

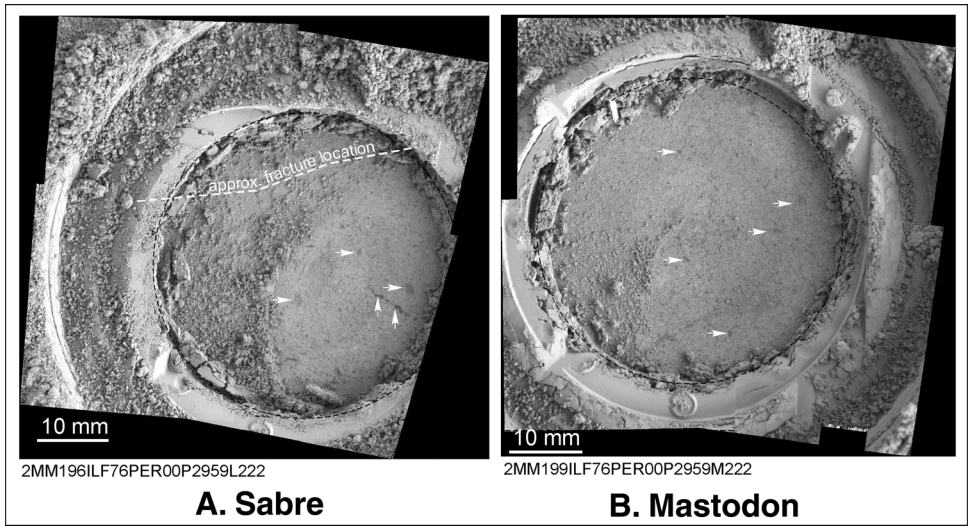

Figure 7. Microscopic images of RAT abraded targets (a) "Sabre" and (b) "Mastodon." Both mosaics were taken when target was fully shadowed. Arrows indicate examples of dark grains or clasts and cracks with adjacent staining. Outcrop fracture intercepted in the area of the preabrasion "Sabre" is not apparent within the abraded RAT hole, while a dark line in the right section may suggest a microfracture.

ments during the Wooly Patch investigation are listed in Table 1.

2.4. Surface Morphology of the Wooly Patch Outcrop Seen in Microscopic Images

[14] The undisturbed surface of Wooly Patch in all three targeted areas (Mammoth, Sabre, Mastodon) was covered by fine-grained dust. The dust appears to have agglomerated into clusters of millimeter to submillimeter size and accumulated mostly in depressions (Figures 6a, 6b, and 6c). Wooly Patch has a network of narrow fractures that divides the rock into multiple sections. Along most of their length, these fractures are straight, but they curve slightly near the edge or corners of the rock and where they cross each other (Figures 4 and 5). All fractures are filled with surface dust (Figures 6a and 6b); thus the fracture depth is unknown. These MI observations confirm those of Pancam and the Hazcams of the fractures in Wooly patch. The MI mosaics of the original surface at Sabre (Figure 6b) show a branched fracture cutting through the field of view. The edges of the fracture and its branches are slightly higher than the rest of the rock surface, suggesting again the hardening of the edges by fluid-involved cementation/deposition. The mor-

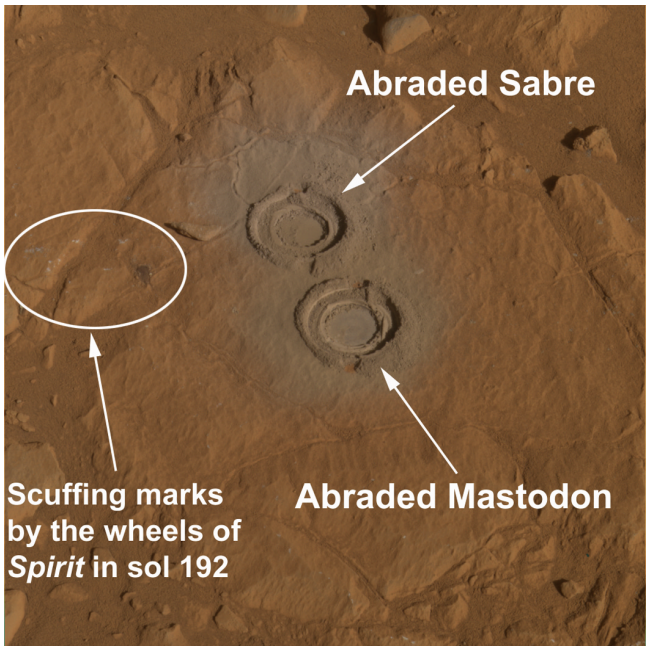

Figure 8. True color Pancam image of Wooly Patch outcrop after abrasions at Sabre and Mastodon. Note the marks in upper left corner of the image by the rover wheeling scuffing. The RAT holes have a diameter ~4.5 cm.

Table 1. Operations and Measurements During the Wooly Patch Investigation

Sol	Rover Instrument	Targets
192	Preapproach Pancam (13 filters)	Wooly Patch outcrop
	Rover approach (west-facing)	Wooly Patch outcrop
193	MI (2 × 1, 5 positions + stereo)	Wooly Patch-Mammoth-asis
	MB (2.5 hrs)	Wooly Patch-Mammoth-asis
	Rover repositioning (south-facing)	Wooly Patch outcrop
194	MI (3 × 3, 5 positions + stereo)	Wooly Patch-Sabre-asis
	MB (2 hrs18 min)	Wooly Patch-Sabre-asis
	APXS (5.8 hrs)	Wooly Patch-Sabre-asis
195	RAT (1 hr 46 min)	WP-Sabre, 5.17 mm depth
196	MI (2 × 2, 5 positions + stereo)	Wooly Patch-Sabre-RAT
	APXS (5.6 hrs)	Wooly Patch-Sabre-RAT
197	MB (21 hrs)	Wooly Patch-Sabre-RAT
	MI (2 × 2, 3 positions + stereo)	Wooly Patch-Mastodon-asis
198	RAT (1hr 41min)	WP-Mastodon, 4.02mm depth
	APXS (5.7 hrs)	Wooly Patch-Mastodon-RAT
199	MI (2 × 2, 3 positions + stereo)	Wooly Patch-Mastodon-RAT
	MB (20 hrs)	Wooly Patch-Mastodon-RAT
200	Rover backup 0.85 m	from Wooly Patch outcrop
	Postbackup Mini-TES	Wooly Patch-Sabre
	Postbackup Mini-TES	Wooly Patch-Mastodon
	Postbackup Mini-TES	Wooly Patch-Sloth-asis
	Postbackup Pancam (13 filters)	Wooly Patch outcrop

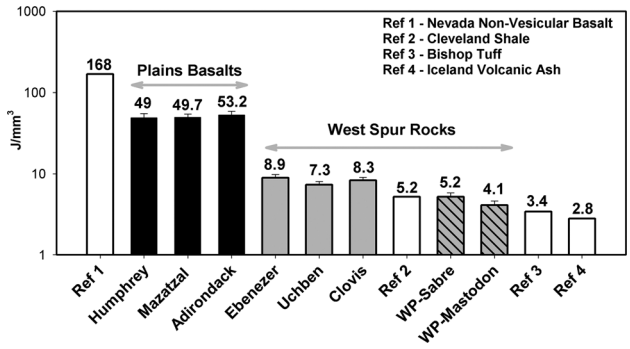

Figure 9. Specific Grinding Energy (SGE) of the Rock Abrasion Tool for the major plains basalts and West Spur rocks at Gusev. SGE values of typical terrestrial rocks are listed for comparison. Note the SGE of plains basalts are only one third of the values for typical terrestrial basalts, and the SGE values of Wooly Patch are the smallest among all Gusev rocks listed.

phologic details of fractures are consistent with the fractures having been conduits for fluid flow at one time.

2.5. Hardness of the Wooly Patch Outcrop Implied by RAT Operations

[15] The telemetry data from the Rock Abrasion Tool (RAT) during the last 0.25 mm of grinding were used to calculate the Specific Grind Energy (SGE in J/mm^3) for each abraded target. This value may be considered as an index of "grindability" and corresponds roughly to the hardness of the material abraded [*Bartlett et al.*, 2005]. The SGE values found for Wooly Patch are 5.15 J/mm^3 at Sabre and 4.11 J/mm^3 at Mastodon (Figure 9). These values are much lower than the SGE values of the plains basalts (49.7–53.2 J/mm^3), which are only about one third of the values for typical terrestrial basalt found during tests in the laboratory. The SGE values of Wooly Patch are among the lowest of all Gusev rocks investigated by Spirit thus far, including some of the highly oxidized West Spur rocks, e.g., Clovis (SGE $\sim$ 8.26 J/mm^3), the low SGE values mean that within the measurement error, Wooly Patch is one of the softest rocks at the Gusev landing site.

[16] Compared to the outcrops at the Meridiani landing site of Spirit's twin rover, Opportunity, Wooly Patch is only slightly harder. Compared to terrestrial analogues, the SGE values of Wooly Patch are within the range of volcanic ash to terrestrial shale (2.8–6.0 J/mm^3) [*Bartlett et al.*, 2005].

2.6. Subsurface Texture of the Wooly Patch Outcrop Exposed by RAT Operations

[17] The target Sabre was placed where a fracture cuts through the original rock surface; whereas the target Mastodon was placed in the middle of a wide section of Wooly Patch, away from any veins and fractures (Figures 5, 6b, and 6c). An MI image of the RAT hole at Sabre taken after grinding (Figure 7a) shows that the original fracture is absent, suggesting that the depth of that fracture was less than 5.17 mm. A dark-toned linear feature (almost straight, indicated by two arrows in Figure 7a) may or may not be one of the micro fractures or veins that originally existed within the matrix of the Wooly Patch outcrop. This dark linear feature could also be staining or spallation along which some of the matrix was plucked by the RAT abrasion.

[18] Both RAT holes at Sabre and Mastodon have extremely fine-grained and light-toned cuttings, evidenced by the fact that they have been pressed into clusters with surprisingly smooth surfaces at the edge of the abraded hole (Figure 7). The MI images also show that the interior of Wooly Patch does not look like the dark and ground-polished abraded surface of the plains basalts (e.g., Humphrey [*Greeley et al.*, 2004, Color Plate 12]). The Wooly Patch subsurface remains light-toned after grinding, consistent with a soft, porous and fine-grained rock matrix.

[19] In MI images, the surfaces of Sabre and Mastodon following abrasion have generally similar characteristics. Between 50–60% of the abraded area of Sabre and 30–40% of Mastodon are obscured by excess grind debris that appears to have dropped from the RAT cutting tool during the removal of the grind head from the rock surface. Where the rock's interior texture is well exposed, the rock appears to consist of a lighter (gray) matrix (too fine-grained to be resolved in MI data, i.e., less than $\sim$0.1 mm) surrounding 10–20% by area of generally equant, darker grains several tenths of a millimeter to one millimeter in diameter (arrows in Figure 7). A few grains appear lighter toned than the matrix. A few of the darker grains have angular margins and the overall impression is that of dark, partially abraded and rounded rock fragments evenly distributed in a finer-grained matrix. Obvious bedding-planes or structure are not identified in either Sabre or Mastodon, but if a section is examined parallel to bedding planes in most sedimentary rocks, the texture may appear relatively structureless depending on the process of sedimentation. On Earth, a similar morphology to the one seen in Wooly Patch might be categorized as a cataclastic rock such as an ash-flow tuff. Figure 10 shows a comparison of the microscale details of a Bandelier ash-flow tuff (from the Valles caldera, NM [*Eichelberger and Koch*, 1979; *Smith and Bailey*, 1966]) with those in the abraded Sabre subsurface.

2.7. Results From Remote-Sensing Investigations

[20] Wooly Patch was imaged, before and after RAT abrasions, with the Pancam 13 "geology" filter set that covers the visible and near infrared wavelength region from

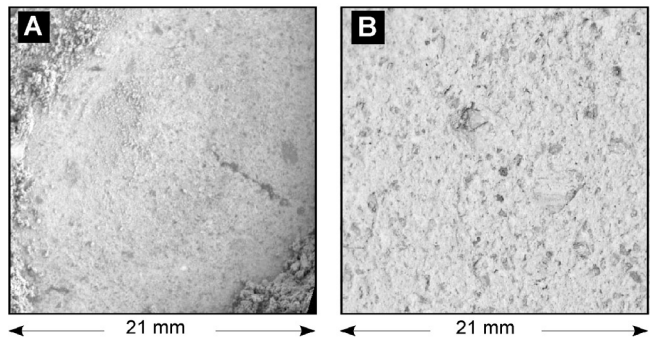

Figure 10. Microscopic details of a Bandolier ash-flow tuff (Figure 10b) compared to the subsurface exposed at abraded Sabre (Figure 10a), which is a partial image from the full MI mosaic of Figure 7a.

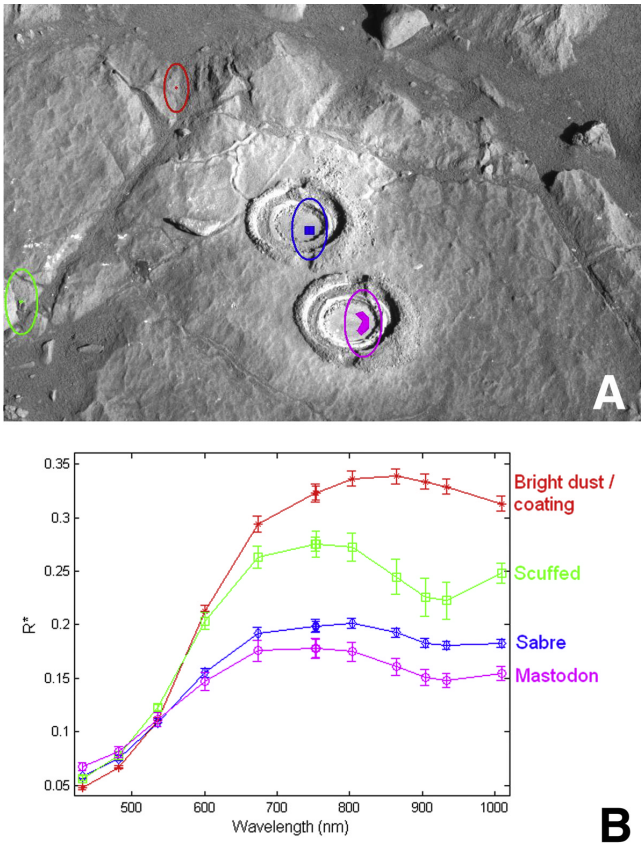

Figure 11. (a) Pcam L5 (535 nm) image and (b) Vis-NIR spectra obtained from undisturbed, scuffed, and abraded areas on Wooly Patch. The areas where the spectra were extracted are color coded the same as the spectra.

430 to 1010 nm [*Bell et al.*, 2003; *Farrand et al.*, 2006]. The spectra extracted from these Pancam images indicate deep spectral absorption features, with a reflectance minimum at 934 nm, in the material exposed in the RAT holes (Figure 11). This spectral feature was deeper in the Mastodon hole than in the Sabre hole. The material exposed in the RAT holes appears spectrally distinct from undisturbed rock. The spectra with the deepest 900 nm absorption feature are from a few patches at the left edge of Figure 11a that were scuffed by Spirit's wheels on sol 192 during its first approach to the Wooly Patch outcrop. The scuffing marks also have a higher albedo than the measurements from the RAT holes. The absorption features in the RAT holes and from the scuffing marks could be produced by either ferric or ferrous iron-bearing minerals; however, the relatively low 535 nm band depth of Wooly Patch is more consistent with a less oxidized ferrous iron-bearing material. Variations in band depth and albedo could be an indication of variability in the materials hosting the Fe-bearing phase, either their oxidation states, or in the grain size of these materials as distributed on the surface of the Wooly Patch outcrop. Spectral parameters of the Wooly Patch RAT holes and scuff marks put it in a spectral class similar to other rocks observed at the base of the West Spur and similar, in terms of its visible and near infrared spectral properties, to a number of Husband Hill rocks [*Farrand et al.*, 2006].

[21] When the Mini-TES spectra from the two abraded targets (Sabre and Mastodon) and one undisturbed area (Sloth) on Wooly Patch were taken after Spirit backed away from the IDD work volume (Table 1), the Wooly Patch rock had been shadowed by Spirit for many sols, and was extremely cold. The rock temperature extracted from the Mini-TES spectra was about 209 K, and the Mini-TES spectra were thus not interpretable.

2.8. Chemistry of Wooly Patch and a Compositional Trend Among West Spur Rocks

[22] The APXS provided the chemical compositions of two targets Sabre and Mastodon on the Wooly Patch outcrop, before and after RAT abrasion. Only the compositions of the abraded rock interior at these targets are listed in Table 2 (based on *Gellert et al.* [2006]). For comparison, we also present compositional data for abraded Adirondack (the first plains basalt investigated by Spirit) and abraded rock at the Clovis outcrop (Table 2). The calculation of FeO and Fe_2O_3 concentration was done on the basis of Mössbauer spectral analysis of Fe^{3+}/Fe_T ratios (Table 3, based on *Morris et al.* [2006]).

[23] Wooly Patch is compositionally distinct from the plains basalts and other West Spur rocks (through sol 304) in that it has the lowest Ca and K concentrations and the highest Al (abraded Sabre) and Ti concentrations. Compared to the plains basalts, Wooly Patch and other West Spur rocks also tend to have higher P and lower Cr and Mn concentrations.

[24] Among West Spur rocks, concentrations of CaO increase linearly with SO_3 from Wooly Patch (low) to Clovis (high; Figure 12). The linear correlation suggests binary mixing between $CaSO_4$ and silicates. Among the abraded West Spur rocks, Wooly Patch represents the silicate extreme whereas Clovis contains the highest amount of sulfates. The abrasion of Pot-of-Gold only removed a small piece from its nodular surface [*Arvidson et al.*, 2006, Figure 13]. The field of view of the APXS covered only a part of the undisturbed surface, thus the data from Pot-of-Gold may be less significant because all other data were derived entirely from the interior of the rocks. Nevertheless, data from undisturbed and brushed surfaces of all West Spur rocks lie along the same linear trend.

[25] Extrapolation of the regression line to zero sulfur suggests that the salt-free portion (silicates) of West Spur rocks contain 3.2 mole% CaO (Figure 12). Extrapolation of the regression line to 100 mole% of SO_3 (corresponding to the SO_3 concentration of gypsum or anhydrite without structural water), yields a CaO concentration of only ~72.5 mole%, suggesting that Ca is not the only cation bound in sulfates at this location. We have found a strong correlation between MgO and SO_3 concentrations (r = 0.998, N = 4) in the compositions of the subsurface regolith exposed in two deep trenches in the plains at Gusev, suggesting the deposition of Mg-sulfate [*Haskin et al.*, 2005; *Wang et al.*, 2005b, 2006]. Mg-sulfates (kieserite), Ca-sulfates (gypsum and bassanite), and polyhydrated sulfates were identified recently by orbital remote-sensing observations (OMEGA-Mars Express [*Arvidson et al.*, 2005; *Bibring et al.*, 2005; *Gendrin et al.*, 2005]). It is thus likely that Mg is also combined with SO_3 at West Spur. If the correlation of the West Spur rocks of Figure 12 is the

Table 2. Compositions of Abraded Wooly Patch Targets Compared With Adirondack and Clovis[a]

Spirit-Sol	A034		A197_S		A199_S		A218_S	
	Adirondack-RAT		WP-Sabre-RAT		WP-Mastodon-RAT		Clovis-Plano-RAT	
Rock-Target	Mass%	±[b]	Mass%	±[b]	Mass%	±[b]	Mass%	±[b]
Na_2O	2.41	0.10	3.33	0.12	2.92	0.10	3.64	0.13
MgO	10.84	0.12	10.92	0.14	11.63	0.13	11.52	0.13
Al_2O_3	10.86	0.12	12.59	0.17	10.34	0.12	8.94	0.10
SiO_2	45.72	0.41	46.82	0.44	46.44	0.43	42.18	0.38
P_2O_5	0.52	0.02	1.24	0.03	1.20	0.03	1.05	0.03
SO_3	1.23	0.03	2.87	0.05	2.41	0.04	7.52	0.10
Cl	0.20	0.01	0.78	0.02	1.03	0.02	1.63	0.03
K_2O	0.07	0.00	0.07	0.00	0.04	0.00	0.35	0.01
CaO	7.75	0.05	3.64	0.04	3.44	0.03	6.04	0.05
TiO_2	0.48	0.01	0.94	0.02	0.91	0.02	0.84	0.02
Cr_2O_3	0.61	0.01	0.27	0.01	0.18	0.01	0.17	0.01
MnO	0.41	0.01	0.10	0.01	0.13	0.01	0.30	0.01
FeO	15.83	0.10	7.00	0.05	7.68	0.05	2.19	0.01
Fe_2O_3	3.35	0.02	10.31	0.07	12.80	0.08	14.96	0.08
NiO	0.02	0.00	0.08	0.00	0.07	0.00	0.09	0.00
ZnO	0.01	0.00	0.01	0.00	0.01	0.00	0.01	0.00
Br	0.00	0.00	0.03	0.00	0.05	0.00	0.02	0.00
Total	100.33		101.00		101.27		101.46	
Fe_3+/FeT (MB)	0.16		0.57		0.6		0.86	

[a]Oxides in mass%.
[b]Calculated on the basis of analytical uncertainty given by APXS team [*Gellert et al.*, 2006].

result of mixing between silicates and Ca- and Mg-sulfates, then the Clovis target contains about 11 mass% Ca- and Mg-sulfates and Wooly Patch contains at most ~4 mass%.

2.9. Fe-Minerals in the Wooly Patch Outcrop Implied by Mössbauer Spectroscopy

[26] The most important features in the Mössbauer spectra of Wooly Patch targets are the extremely low intensities of the spectral doublet assigned to Fe^{2+} in olivine (Table 3) [*Morris et al.*, 2006, Figure 2e], which was very prominent in all Gusev plains basalts and soils before Spirit reached West Spur [*Morris et al.*, 2004]. The strongest Fe^{2+} spectral doublet in the spectra of Wooly Patch (and other West Spur rocks) is assigned to octahedrally coordinated Fe^{2+} cations. This doublet is similar to the Fe^{2+} component (Fe2D2 in Table 1 of *Morris et al.* [2006]) assigned to pyroxene in plains basalt, but having slightly different Mössbauer parameters, especially a larger quadrupole splitting (2.17 ± 0.02 mm/s for abraded Mastodon; 2.49 ± 0.02 mm/s for abraded Ebenezer, another West Spur rock), relative to 2.04 ± 0.02 mm/s of Fe^{2+}_Px doublet in Adirondack [*Morris et al.*, 2006]. Analyses of Mössbauer data are still ongoing to support a detailed and conclusive mineral identification. Phyllosilicates are possible on the basis of previously published Mössbauer parameters [*Görlich et al.*, 1989; *Gunter et al.*, 1984; *Matsui et al.*, 1972].

[27] There are three sets of spectral sextets, of which two could be assigned to magnetite and one to hematite with

Table 3. Results of the Mössbauer Spectral Analysis for Component Areas and Redox State[a]

Sample Name	Phase Assignment							
	Ol	Px[b]	np	Mt	Hm	Ilm	Gt	Fe^{3+}/Fe_T
A034 Adirondack-Blue-RAT	49	32	5	13	0	0	1	0.16
A193 Wooly Patch_Mammoth4	5	48	18	11	16	1	2	0.46
A195_S Wooly Patch-Sabre-asis	6	31	29	16	14	0	3	0.58
A197_S Wooly Patch-Sabre-RAT	3	34	25	17	17	1	3	0.57
A199_S Wooly Patch-Mastodon-RAT	2	32	29	16	12	1	9	0.6
A218_S Clovis-Plano-RAT	2	11	26	2	18	0	40	0.86

[a]Component areas given in %. Ol, olivine; Px, pyroxenes; np, nanophase Fe^{3+}oxide; Mt, nonstoichiometric magnetite; Hm, hematite; Ilm, ilmenite; Gt, goethite. Component uncertainties range from ±2 to ±4, Fe^{3+}/Fe_T uncertainty is ±0.04 (f-factor corrected).
[b]Mössbaeur parameters of "pyroxene" phase in Wooly Patch targets are different from those of other rocks.

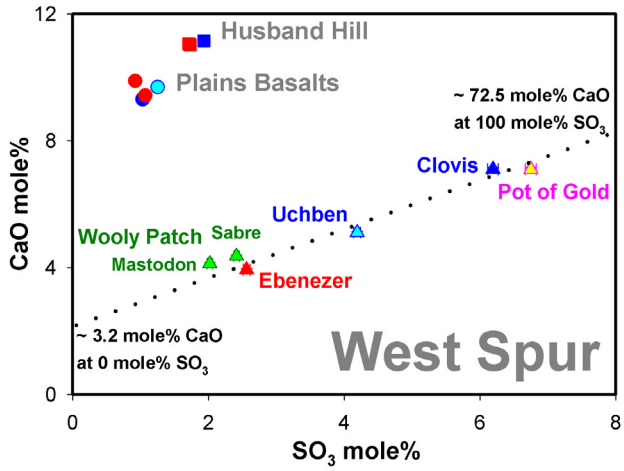

Figure 12. Among abraded West Spur rocks (triangles), CaO concentrations correlate strongly with SO_3 concentrations ($r = 0.982$, $N = 6$, while r = 0.917 is significant at 99% confidence level). For comparison, data for abraded plains basalts and two Husband Hill rocks (Wishstone and Champagne) are also shown. The Wooly Patch samples are at the silicate-rich extreme of the mixing trend. We infer that another end-member of this mixing trend is a sulfate component, i.e., Ca, Mg-sulfates with a Ca/(Ca+Mg) ratio ~0.725.

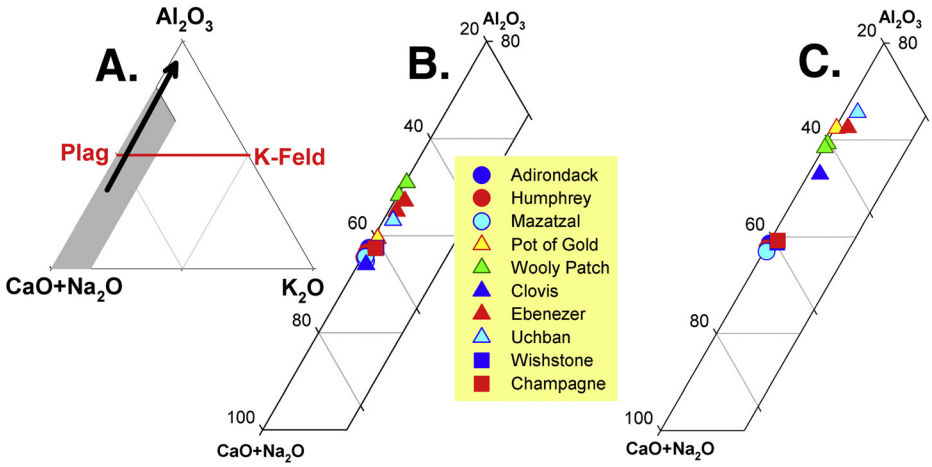

Figure 13. (a) Al_2O_3 - $CaO+Na_2O$ - K_2O ternary diagram. The arrow indicates the chemical weathering trends found in the Baynton profile from Australia [*Nesbitt and Wilson*, 1992], Casino profile from Australia [*Brain and Russell*, 1980], and Morvern profile from Scotland [*Craig and Loughnan*, 1964]. These are all basaltic rocks with phyllosilicate minerals as the products of chemical weathering. The shadowed area is shown in Figures 13b and 13c. Plag, plagioclase; K-feld, K-feldspar. (b) The compositions of abraded West Spur rocks compared with three plains basalts and two Husband Hill rocks in Al_2O_3 - $CaO+Na_2O$ - K_2O ternary diagram. The abraded Sabre and Mastodon targets on Wooly Patch (light green triangles) are Al-rich end-members in this chemical trend. (c) After removing the percentage of ions associated with salts and Fe-oxides/hydroxides assigned by Mössbauer analysis and chemical correlations, all rocks on West Spur form a linear trend similar to the chemical weathering trend of terrestrial plutonic and volcanic rocks.

approximately equal peak areas. The major Fe^{3+} spectral doublet is assigned to nanophase Fe^{3+} (e.g., oxides or oxyhydroxides), which is interpreted as an alteration product at Gusev. This doublet is observed to be strong in the undisturbed surface soils, the surface dust and coherent rock coatings, and those targets also show an Fe^{3+} absorption edge in Pancam spectra and dusty features in Mini-TES spectra [*Bell et al.*, 2004; *Christensen et al.*, 2004; *Morris et al.*, 2004]. Mössbauer spectral deconvolution suggests small amounts of goethite in each of the Wooly Patch targets; abraded Mastodon has the highest amount.

[28] All targets (as-is and abraded surfaces) of Wooly Patch are more oxidized ($Fe^{3+}/Fe_T \sim 0.46-0.61$) than the plains basalts and general Gusev surface soils, but less oxidized than most of the West Spur rocks, e.g., Clovis ($Fe^{3+}/Fe_T \sim 0.83-0.85$) where a large quantity of crystalline goethite (40% Fe) was identified [*Morris et al.*, 2006]. In comparison to Clovis, most of the Fe^{3+} in Wooly Patch resides in hematite and nanophase oxides, not in goethite. In contrast to plains basalts, the targets within the interior matrix of Wooly Patch are more oxidized than the as-is surface, i.e., Mammoth. The as-is surface at Sabre, where a fracture cut through the field of view of the IDD instruments (Figure 6b), is at the same oxidation level as the rock interior, with a slightly higher proportion of ferric nanophase oxides and a lower proportion of hematite than the subsurface material (Table 3).

3. Analyses for Silicate Mineralogy of Wooly Patch

[29] In order to understand the mineralogy and geochemistry of the Gusev rocks, we would ideally employ four analysis methods on the same set of APXS and Mössbauer data. The four methods are (1) comparison of cation molar ratios; (2) CIPW normative mineralogy calculation; (3) mass balance mixing calculations; and (4) olivine calculation based on APXS data and the $Fe^{2+}_{olivine}$ and Fo# estimation by Mössbauer analysis. We would then compare the results from these analyses with each other for consistency, and, if available, with the mineral proportions produced from the Mini-TES spectral deconvolution of the same target. For the Wooly Patch investigation, only 2–3 mass% of Fe is assigned by Mössbauer analysis to $Fe^{2+}_{olivine}$ in the rock interior, and the Mini-TES observation provides uninterpretable spectra owing to the low temperature of the rock. Thus, in the following sections we employ only methods (1), (2), and (3).

3.1. Comparison of Cation Molar Ratios

[30] In addition to the silicate-sulfate trend, the compositions of Wooly Patch appear at the extremes in two other compositional trends. *Nesbitt and Young* [1984] used an Al_2O_3 – $(CaO+Na_2O)$ – K_2O ternary diagram to evaluate the weathering trend of plutonic and volcanic rocks based on thermodynamics and kinetics. They found that weathering processes (involving either crystalline mineral phases or glassy materials) are expressed by linear trends from the $(CaO+Na_2O)$-rich end toward the Al_2O_3 apex, subparallel to $(CaO+Na_2O)$ – Al_2O_3 boundary in most cases (Figure 13a). This trend is caused mainly by the higher alteration rate of plagioclase than K-feldspar, i.e., the removal of Ca and Na drives the composition toward gibbsite and kaolinite. The linear trend will bend away from the K_2O apex when a high degree of alteration occurs in which K is leached from K-feldspar [*Nesbitt and Young*, 1984].

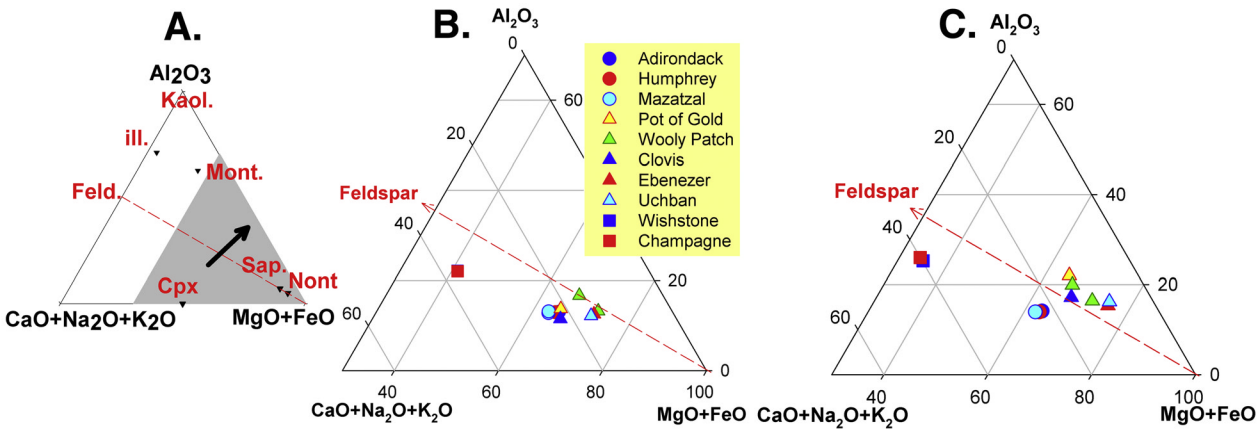

Figure 14. (a) Al_2O_3 - $CaO+Na_2O+K_2O$ - $FeO+MgO$ ternary diagram. The arrow indicates the chemical weathering trends found in Baynton, Casino, and Morvern. The compositions of igneous rocks occur in the region below the jointing line joining the feldspar composition to the MgO+FeO apex. Chemical weathering drives compositions to the region above the red line. The shadowed area is shown in Figure 14b and 14c. Kaol, kaolinite; ill, illite; Mont, montmorillonite; Sap, saponite; Nont, nontronite; Cpx, clinopyroxene; Feld, feldspar. (b) Abraded West Spur rocks compared with the plains basalts and two rocks on Husband Hill. Abraded Sabre and Mastodon on Wooly Patch is on the line separating igneous rocks and chemical weathering products. (c) After removing the percentage of ions associated with salts and Fe-oxides/hydroxides assigned by Mössbauer analysis and chemical correlations, the silicate-only compositions of West Spur rocks occur in the region of chemical weathering products (above the red line).

[31] Compositions of abraded Sabre and Mastodon lie at the Al_2O_3-rich extreme of the linear trend defined by Gusev rocks (though sol 356) in the Al_2O_3 – ($CaO+Na_2O$) – K_2O ternary diagram, while the compositions of plains basalts lie at the $CaO+Na_2O$-rich extreme (Figure 13b). Given that some West Spur rocks contain >13 mass% salts, especially Ca-sulfate, the best way to evaluate the silicate alteration of these rocks is to remove mathematically the portions of ions associated with the salts. To account for the presence of salts and Fe-oxides and Fe-hydroxides, we used the following calculation procedure. First, the mass% of Fe assigned to Fe-oxides and Fe-hydroxides by Mössbauer analysis is subtracted from the total Fe mass% value from the APXS measurement. Then as a first approximation, portions of Na are stochiometrically associated with total Cl, and portions of Mg and Ca are associated with total S to make chlorides and sulfates as salt components in these rocks. These portions are then subtracted from the APXS compositions. For all Gusev rocks, we associate a portion of Na to Cl (to make NaCl); for plains basalts and for the two rocks (Wishstone & Champagne) on Husband Hill, we associate a portion of Mg to S (to make $MgSO_4$); and for the West Spur rocks, we associate portions of both Ca and Mg to S, using a Ca/(Ca+Mg) ratio of 0.725 based on the linear regression line in Figure 12 (to make $MgSO_4$ and $CaSO_4$). Informed assumptions are used to make these associations. These assumptions are based either on MER observations (Figure 12) [e.g., *Ming et al.*, 2006, Figure 8] or on observations of compositional trends in other surface analyses, e.g., Viking and Pathfinder [*Larsen et al.*, 2000; *McSween*, 2005], or they are based on the fact that a uniform association (e.g., Na to Cl for all rocks) for the salts will not affect a qualitative comparison of silicates. When we plot the renormalized silicate-only compositions of these rocks on the Al_2O_3 – ($CaO+Na_2O$) – K_2O ternary diagram (Figure 13c), we find that West Spur rocks are more Al-rich and well separated from the plains basalts and the two rocks on Husband Hill. The West Spur rocks also form a linear trend similar to those found by *Nesbitt and Young* [1984] in chemical weathering of terrestrial plutonic and volcanic rocks.

[32] *Nesbitt and Wilson* [1992] used an Al_2O_3 – $CaO+Na_2O+K_2O$ – FeO_T+MgO ternary diagram (Figure 14a) to illustrate weathering trends of three terrestrial basaltic rocks: Baynton profile [*Nesbitt and Wilson*, 1992] and Casino profile [*Craig and Loughnan*, 1964] from Australia, and Morvern profile from Scotland [*Brain and Russell*, 1980]). All of these have phyllosilicate minerals as products of chemical weathering, and they all show a weathering trend from a composition enriched in feldspar, pyroxene, and olivine (the region below the feldspar – FeO_T+MgO join in Figure 14a) toward an Al-enriched composition (i.e., toward the Al_2O_3 – FeO_T+MgO boundary in Figure 14a). In these cases, the trend is almost perpendicular to the join. These trends indicate leaching of Ca, Na, and K from feldspar, as well as Mg and Fe from olivine and pyroxene during the chemical weathering of these basalts. When weathering products dominate, the corresponding rock compositions occur in the region above the feldspar–FeO_T+MgO join in the ternary diagram where most chemical weathering minerals occur.

[33] We note that comparing to the plains basalts and the two rocks from Husband Hill, the compositions of Wooly Patch outcrop appear to be Al-rich in the Al_2O_3 – $CaO+Na_2O+K_2O$ – FeO_T+MgO ternary diagram and occur on the feldspar–FeO_T+MgO join (Figure 14b). After the

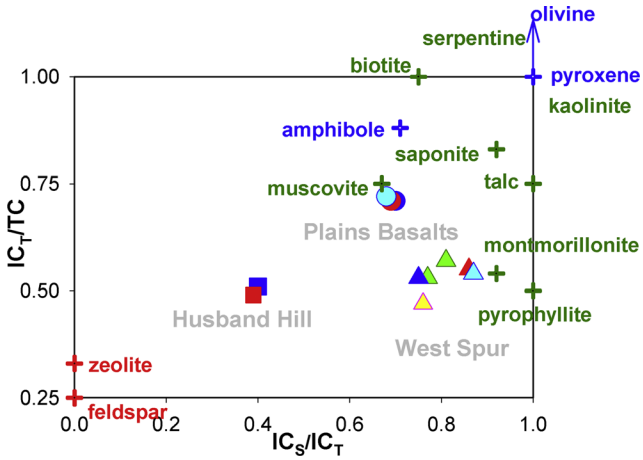

Figure 15. A comparison of the molar ratios of major cations of the abraded rocks at West Spur (triangles) with three plains basalts (circles) and two of Husband Hill rocks (Wishstone and Champagne, squares). The molar ratios were derived from APXS elemental mass%, with a set percentage of Fe assigned to Fe-oxides and Fe-hydroxides (from Mössbauer analysis), and the percentage of Na, Mg, and Ca assigned to chlorides and sulfates (determined by elemental correlations) removed. Data for the West Spur rocks spread over a wide range, indicating chemical alteration. When compared with the molar ratios of silicate minerals of different degrees of polymerization, the positions of West Spur rocks suggest addition of silicates with mid-range polymerization, i.e., phyllosilicates.

removal of those percentages of Fe, Ca, Mg, and Na associated with chlorides, sulfates, Fe-oxides and Fe-hydroxides, as described previously, the compositions of all West Spur rocks plot above the feldspar–FeO+MgO join, thus indicating a weathering signature (Figure 14c).

[34] A cation ratio plot of IC_T/TC versus $IC_S/(IC_S+IC_L)$ (Figure 15) is an alternate means to assess the silicate mineralogy. TC is the molar sum of tetrahedral cations (i.e., Si, Al), which form the structural framework of silicate minerals. IC_T is the molar sum of all interstitial cations (i.e., Mg, Fe, Mn, Ca, Na, K), which fill the regular and irregular interstitial sites (among the Si/Al-O_4 tetrahedra) of the silicates. Among all interstitial cations, IC_S represents those with a small cation radius (i.e., Mg, Fe, Mn), which normally fill regular octahedral sites in ortho-, chain-, and layer-silicates. IC_L represents those with a large cation radius (Ca, Na, K), which can only fit into the large polyhedral sites between the layers in phyllosilicates, the central space in ring-silicates, and the large spaces formed by the Si/Al - O framework in tectosilicates (e.g., feldspars or zeolites). A cation ratio plot of IC_T/TC versus $IC_S/(IC_S+IC_L)$ provides first order information on the degree of polymerization of the silicates and helps assess the type of silicate mineralogy (ortho-, chain-, layer-, and tectosilicate) that contributes to a rock composition when the mineralogy is unknown. Using this plot, the tectosilicate class can be overestimated, however, because of the uncertainty in the site occupancy of Al, which is located in tetrahedral sites in tectosilicates but mostly occupies octahedral sites in chain and layered-silicates. For the purpose of assessing the silicate mineralogy of Gusev rocks, those percentages of Fe, Ca, Mg, and Na that could be associated with chlorides, sulfates, Fe-oxides and Fe-hydroxides were subtracted from the compositions, as previously described, and the renormalized compositions are plotted.

[35] In a IC_T/TC versus IC_S/IC_T plot, the composition of plains basalts and Husband Hill rocks are tightly clustered within their own groups (Figure 15), consistent with a distinct and different origin for each group. The compositions of West Spur rocks, however, spread over a much wider range. If there were a single origin for West Spur rocks, their compositions, especially the major cations for their silicate mineralogy, may have been altered by processes such as chemical weathering or hydrothermal alteration.

[36] Compared to the two other groups, West Spur rocks have a slightly higher proportion of tetrahedral cations (especially Al) than the plains basalts, and lesser proportions of large interstitial cations (Ca, Na, K) than Husband Hill Wishstone-Champagne rocks. The major difference between West Spur rocks appears to be the ratio of small-sized interstitial cations IC_S to large-sized interstitial cations IC_L, such as the low Ca concentration in Wooly Patch compositions. In Figure 15, we mark the general positions of typical silicates of different degrees of polymerization for comparison, and we use NBO values (the number of non-bridging oxygen atoms) to quantify the degree of polymerization (Table 7). The higher NBO values (4–1.5) correspond to the lower degree of polymerization (olivine, pyroxene, and amphibole). NBO equals zero for fully polymerized silicates (feldspars and zeolites). Phyllosilicates (mica, smectite, talc, kaolinite, and serpentine) are the intermediates, with NBO values equal to one. Among three types of Gusev rocks compared in this plot, plains basalts contain olivine, pyroxene and feldspar as major silicates (e.g., Adirondack in Table 4). Their data points lie along a line that connects the points of pyroxene and feldspar, and are toward the pyroxene end, whereas the data points of two Husband Hill rocks lie along the same line but are toward the feldspar end. These data locations suggest that the silicate mineralogy in these rocks could be very similar, with a major difference in the relative proportions of minerals that have no NBO, i.e., feldspar. In contrast, the data points of West Spur rocks lie away from the pyroxene-feldspar line, and are scattered in the field of some phyllosilicates. The locations of these data points indicate additional silicate phases with intermediate polymerization and low NBO values (but not zero). Phyllosilicates are plausible candidates.

3.2. Normative Mineralogy Calculations

[37] We have employed a modified CIPW [*Cross et al.*, 1902] normative mineralogy calculation to estimate the silicate mineralogy of the Wooly Patch outcrop. A standard set of igneous minerals is used in these calculations [*Cross et al.*, 1902], but modifications reflect cation assignments to salts and Fe to Fe-oxides based on Mössbauer analysis, in order to isolate the silicate mineralogy. This calculation was first applied to a well-studied plains basalt, Adirondack. The normative mineral proportions we obtained (Table 4) are almost identical to those obtained by *McSween et al.* [2006], and the derived ratio of olivine/(olivine + pyroxene) is also very similar to the ratio of fayalite/(fayalite + Fe^{2+}_px) by

Table 4. Mineral Proportions Obtained From a Modified Normative Calculation Based on Basaltic Mineralogy

RAT Abraded Rocks	Adirondack-RAT	Wooly Patch-Sabre	Wooly Patch-Mastodon	Clovis-Plano
Halite	0.3	1.2	1.6	2.6
Mg-Sulfate	1.8	1.1	0.9	3.0
Ca-Sulfate	0.0	3.2	2.8	8.8
Ca-Phosphate	1.8	3.9	3.8	3.4
Chromite	0.9	0.4	0.2	0.2
Ilmenite	0.9	1.6	1.6	1.5
Fe_3O_4	2.8	2.7	3.1	0.3
Fe_2O_3	0.2	3.3	3.4	9.6
K-feldspar	0.4	0.4	0.2	2.0
Na-feldspar	18.8	20.6	15.9	17.8
Ca-feldspar	19.3	2.5	2.9	3.9
Diopside	12.1	0.0	0.0	0.0
Mg, Fe – pyroxene	18.6	39.9	46.9	34.9
Mg, Fe – olivine	22.1	0.0	0.0	0.0
Al_2O_3		**13.2**	**10.9**	**6.5**
SiO_2		**5.9**	**5.8**	**5.5**
Mg#	**0.47**	0.67	0.62	0.77
An#	**0.51**	0.11	0.16	0.18
Norm obtained Ol/(Px + Ol)	**0.61**			
MB obtained Fe^{2+} [Ol/(Px + Ol)]	**0.60**			

Mössbauer analyses (Table 4). We have made similar calculations for the two abraded targets (Sabre and Mastodon) on Wooly Patch and one abraded target "Plano" on Clovis (Table 4). The normative analysis reveals that both Wooly Patch targets have excess SiO_2 and Al_2O_3 relative to basaltic mineralogy. *Ming et al.* [2006] have also noted that West Spur rocks contain normative corundum (i.e., excess Al_2O_3). We note that the excesses of SiO_2 and Al_2O_3 in these targets are not affected by the selection of cations carried by salts, e.g., either Na or K, or both for chlorides, and either Ca or Al for phosphates. In other words, basaltic mineralogy plus minor chlorides and sulfates cannot account for the chemical compositions of the rock matrix within Wooly Patch, nor for those of the rock Clovis. The excesses of SiO_2 and Al_2O_3 in the normative mineralogy of Wooly Patch require additional silicates with higher degree of polymerization, as indicated by the IC_T/TC versus IC_S/IC_T plot in Figure 15. It is also clear that the conventional normative mineralogy calculation is not suitable for identifying the additional polymerized silicates in Wooly Patch. Therefore we adopt an approach that was initially guided by a cation ratio comparison, and then tested using a linear mass balance mixing-model calculation.

3.3. Weighted Least Squares Mass Balance ("Mixing Model")

[38] "Mixing models," that is, weighted, least-squares-mass-balance calculations, provide an alternate approach to calculating the mineralogy of a rock, given some knowledge of, or assumptions about, the possible mineral end-member compositions. Input parameters include (1) the chemical composition (concentrations of elements) of a mixture or assemblage of minerals, (2) the compositions, known or assumed, of a set of known or assumed components of the mixture or assemblage, and (3) a weighting factor for each element. The weighting factor accounts for the reality that some elements provide a better constraint on mass balance than others because their concentrations are known more precisely (in both mineral end-members and in the unknowns) or the element is more abundant. The solution to the least squares equation is the mass fraction, f_i, of each component i that accounts best for the composition of the mixture or assemblage as well as a goodness-of-fit parameter, χ^2/ν (reduced chi-square, the weighted, least squares sum-of-residuals). If the number of components equals the number of elements, then an explicit solution could be calculated. In most geologic problems where compositional mass balance is useful, however, the system is overdetermined in that there are more chemical elements than components; thus a least squares approach is required. Computational details of the model approach used here are given in [*Korotev*, 1997; *Korotev et al.*, 1995].

[39] Ideally, mixing models are applied to systems where the mineralogical or lithological components of a rock or mixture are known. In this mode, the purpose of the modeling is to find the relative proportions of the components that best accounts for the composition of the mixture [e.g., *Korotev and Kremser*, 1992]. The approach, however, can also be useful when the identities of components are not well known. When used in this mode, many different sets of assumed components are tested to determine which sets best account for the composition being modeled [e.g., *Burbine and O'Brien*, 2004; *Korotev*, 1997]. It is in this mode that we use the mixing-model approach here. Mixing models cannot prove that a set of assumed components is, in fact, the actual set of components of a mixture or assemblage because any of a number of such sets may be able to account for mass balance, including some not anticipated or tested. Mixing models, however, can demonstrate that particular sets do not account for mass balance. "Good fits" are those for which (1) χ^2/ν is small in value, (2) Σf_i is approximately unity (the model calculations do not constrain the sum of components to be 100%), (3) no negative values of f_i occur in the best-fit solution, and (4) the best-fit solution is geologically reasonable.

[40] The APXS instrument provides atomic mass percentages of 16 elements. For our analysis of major silicate mineralogy, no effort was made to account for Ni, Zn, Mn, and Br, which are in low concentration and thus do not

provide important constraints to mass balance of the silicate mineralogy. Therefore only minerals consisting of any of the 12 elements Na, Mg, Al, Si, P, S, Cl, K, Ca, Ti, Cr, and Fe were used in the modeling, which limits the number of mineral components used to account for mass balance to 12 or less. On the basis of geochemical and mineralogical considerations we tested numerous sets of minerals using the mixing-model approach.

3.3.1. Special Constraints Used for Wooly Patch Analyses

[41] Mass balance considerations are not useful for distinguishing among several components that are similar in composition (e.g., magnetite, hematite, goethite, etc.) or when compositions of some components are mathematically equivalent to mixtures of others (olivine + quartz = pyroxene). Fortunately, Mössbauer analysis has provided detailed information on Fe-oxides and Fe-hydroxides [*Morris et al.*, 2004, 2005, 2006], and the emphasis of our analysis is the silicate mineralogy. We therefore select to not include Fe-oxides and Fe-hydroxides in the calculations. We removed the mass% of Fe in APXS data as assigned by Mössbauer analysis to Fe-oxides and Fe-hydroxides, and used the renormalized compositions for the calculation.

[42] For the major elements, Mg, Al, Si, Ca, and Fe, we used the reported accuracy (standard deviation, σ_i) of each element i from the APXS calibration [*Gellert et al.*, 2004, 2006] in the weighting factor ($1/\sigma_i^2$). For Na, however, we used 20% of the concentration value instead of the reported uncertainty in the accuracy, 8.5%, because of the poor precision of derived Na mass% values caused by a spacecraft hardware issue [*Gellert et al.*, 2004]. For the remaining elements determined by the APXS, S, Cl, Cr, Ti, and P, concentrations are low for Wooly Patch targets compared with some Gusev subsurface soils. For the purpose of the modeling, we make the simplifying assumption that all S is quantitatively carried by Ca,Mg-sulfates, all Cl is in halite, all Cr is in chromite, all Ti is in ilmenite, and all P is in Ca-phosphates. Although the relative analytical uncertainties are large, we nevertheless weighted these five minor elements heavily in order to account stochiometrically for the reported concentrations. Among the assumed minor and salt phases, we have positive constraints on Ca, Mg-sulfates by compositional correlation and identification of ilmenite by Mössbauer analysis. We have no direct mineralogical evidences for halite, apatite and chromite. We have tested and concluded that the selections of cations in these phases (e.g., either Na or K or both for chlorides, and either Ca or Al for phosphates) do not significantly affect the silicate mineralogy inferred from the model because of the low concentrations of S, Cl, Cr, Ti, and P in Wooly Patch targets.

[43] Information on hydrogen and oxygen is not available at the present time from the APXS results; thus the atomic mass% values for water-bearing minerals used in the standard mineral set were renormalized to a water-free basis. The final mineral modes (mass%) were converted to a water-bearing basis for water-bearing minerals.

3.3.2. Standard Mineral Sets Selected and Tested for Wooly Patch

[44] We have selected and tested 145 sets or combinations of minerals (Table 5) to account for the compositions of Wooly Patch (Table 3). Seven sets have basaltic minerals only, and 138 sets have combinations of basaltic minerals and alteration-related minerals, especially phyllosilicates. Among them, 64 sets involve smectites, 32 sets involve talc-pyrophyllite group minerals, and 42 sets involve kaolinite-serpentine group minerals.

[45] Assuming that basaltic materials were the likely starting materials for the rocks and soils at Gusev, we included basaltic mineral phases in each of the alteration mineral sets. During the subsequent trials, we gradually removed the basaltic minerals from the mineral set until the lowest χ^2/ν (best least-squares fit) was obtained. The order we used to remove the primary basaltic minerals was based on the established dissolution rates of basaltic minerals in an acidic environment [*Blum and Stilling*, 1995; *Grandstaff*, 1977; *Knauss et al.*, 1993; *Pokrovsky and Schott*, 2000a, 2000b; *Schott et al.*, 1981; *Wogelius and Walther*, 1992], i.e., first olivine, then Ca-rich pyroxene and Ca-feldspar, and MgFe-pyroxene and K-feldspar as the last.

[46] Smectites are the most commonly suggested phyllosilicates for Mars rocks [*Burns and Fisher*, 1990; *Gooding*, 1992; *Huguenin*, 1974]. Nontronite (Fe-smectite) was identified by the OMEGA instrument on the Mars Express orbiter [*Bibring et al.*, 2005]. We used two groups (32 sets for each) of smectite-bearing mineral assemblages, in which typical terrestrial smectite (TT-smectite) and end-member smectite (EM-smectite) were used respectively. A low Na/Ca ratio was used in the TT-smectite group on the basis of the compositional values collected by *Deer et al.* [1963], in which Ca-end-member montmorillonite has a formula of $[(Na_{0.08}Ca_{0.29})(Mg_{0.66}Al_{3.34})\ Si_8O_{20}(OH)_4{\cdot}2H_2O]$, Mg-end-member saponite has $[(Na_{0.08}Ca_{0.29})Mg_6(Si_{7.34}Al_{0.66})O_{20}(OH)_4{\cdot}2H_2O]$, and Fe-end-member nontronite has $[(Ca_{0.33})Fe_4(Si_{7.34}Al_{0.66})O_{20}(OH)_4{\cdot}2H_2O]$. In another 32 smectite-bearing mineral assemblages, EM-smectites were used in order to cover a wide range of potential chemical variations on Mars and minerals of different types but having similar compositions. The same nontronite composition is used for the Fe-end-member, but a Ca-rich montmorillonite $Ca_{0.33}(Mg_{0.66}Al_{3.34})Si_8O_{20}(OH)_4{\cdot}2H_2O]$ and a Na-rich saponite $[Na_{0.66}Mg_6(Si_{7.34}Al_{0.66})O_{20}(OH)_4{\cdot}2H_2O]$ were used for Ca- and Mg-end-members. When using the EM-smectite group, the compositional range covers minerals such as beidellite, hectorite, sauconite, and vermiculite (Table 7). Our calculations show that the variation in Na/Ca between the TT-smectite and EM-smectite groups does not affect the general trend in silicate mineralogy. (In Figure 16, the data positions and data patterns among TT-smectite and EM-smectite fields partially reflect this finding.)

[47] Dehydrated smectite-group minerals have the same structure and the same Mg/Si, Al/Si, and Fe/Si ratios as the minerals in the talc-pyrophyllite group, because both groups have the same IC_T/TC ratio ~2/4 (with trivalent cations) or ~3/4 (with divalent cations, Table 7). For this reason, we selected and tested the talc-pyrophyllite group minerals (to represent the dehydrated smectite minerals in the mixing-model analysis, understanding that some smectite minerals could keep certain hydration states under current Mars surface conditions [*Bish et al.*, 2003]). The standard chemical formula used for talc-pyrophyllite group minerals is $[X_{3or2}(Si_4O_{10})(OH)_2]$, where talc, pyrophyllite, and minnesotaite are the three compositional end-members, and where X represents Al, Mg, and Fe. Different combinations of these hydrated minerals and anhydrous basaltic minerals

Table 5. Mineral Assemblages Used for Mass Balance Mixing Model Calculations for Wooly Patch Targets[a]

Basaltic Minerals Only (7 Sets)[b]	Typical Terrestrial (TT) Smectites and Igneous Minerals (32 Sets)[c]	End-Member (EM) Smectites and Igneous Minerals (32 Sets)[d]	Talc-Pyrophyllite-Minnesotaite and Igneous Minerals (32 Sets)[e]	Kaolinite-Antigorite-Greenalite and Igneous Minerals (42 Sets)[f]
Or_Ab_An_En_Fs_Fo_Fa	Mon_Sap_Non only	Mon_Sap_Non only	Talc_Pyr_Min only	Ka_Ant_Gre (2) only
Or_Ab_An_Di_En_Fs	Mon_Sap_Non _Or_Ab_An	Mon_Sap_Non_Or_Ab_An	Talc_Pyr_Min_Or_Ab_An	**Kao_Ant_Gre (2)_Or_Ab_An**
Or_Ab_An_En_Fs	Mon_Sap_Non _Or_Ab	Mon_Sap_Non _Or_Ab	Talc_Pyr_Min_Or_Ab_An_Di_En_Fs	Kao_Ant_Gre (2)_Or_Ab
Or_Ab_En_Fs	Mon_Sap_Non _Or_Ab_Di	Mon_Sap_Non _Or_Ab_Di	Talc_Pyr_Min_Or_Ab_An_En_Fs	Kao_Ant_Gre (2)_Or_An
Or_Ab_Di_En_Fs	Mon_Sap_Non _Or_Ab_En_Fs	Mon_Sap_Non _Or_Ab_En_Fs	Talc_Pyr_Min_Or_Ab_An_En	Kao_Ant_Gre (2)_Ab_An
Or_Ab_An	Mon_Sap_Non _Or_Ab_Fs	Mon_Sap_Non _Or_Ab_Fs	*Pyr_Min_Or_Ab_An_En*	**Kao_Ant_Gre (2)_Or_Ab_An_Qtz**
Or_Ab_An_Fo_Fa	*Mon_Sap_Or_Ab_Fs*	*Mon_Sap_Or_Ab_Fs*	Talc_Pyr_Min_Or_Ab_Di_En_Fs	Kao_Ant_Gre (2)_Or_Ab_An_Di_En_Fs
	Mon_Non_Or_Ab_En	Mon_Non_Or_Ab_An_En	Talc_Pyr_Min_Or_Ab_Di_En	Kao_Ant_Gre (2)_Or_Ab_An_En_Fs
	Mon_Sap_Non _Or_Ab_Fo_Fa	***Mon_Sap_Non_Or_Ab_An_Fo_Fa***	Pyr_Min_Or_Ab_Di_En	Kao_Ant_Gre (2)_Or_Ab_An_En
	Mon_Sap_Non _Or_Ab_Fa	Mon_Sap_Non _Or_Ab_An_Fa	Talc_Pyr_Min_Or_Ab_An_Fo_Fa	**Kao_Gre_Or_Ab_Di_En**
	Mon_Sap_Or_Ab_Fa	***Mon_Sap_Or_Ab_An_Fa***	Talc_Pyr_Min_Or_Ab_An_Fo	Kao_Ant_Gre (2)_Or_Ab_An_Fs
	Mon_Non_Or_Ab_Fo	***Mon_Non_Or_Ab_An_Fo***	***Pyr_Min_Or_Ab_An_Fo***	**Kao_Ant_Or_Ab_Di_Fs**
	Mon_Sap_Non _Di_En_Fs	Mon_Sap_Non _Di_En_Fs	Talc_Pyr_Min_Di_En_Fs	**Kao_Ant_Gre (2)_Or_Ab_Di**
	Mon_Sap_Non _Di_Fs	Mon_Sap_Non _Di_Fs	Talc_Pyr_Min_En_Fs	**Kao_Ant_Gre (2)_Or_Ab_Di_Qtz**
	Mon_Sap_Di_Fs	Mon_Sap_Di_Fs	Pyr_Min_En_Fs	Kao_Ant_Gre (2)_Or_Ab_An_Fo_Fa
	Sap_Fs	Mon_Sap_Fs	Pyr_En_Fs	Kao_Ant_Gre (2)_Or_Ab_An_Fo
	Mon_Sap_Non _Fo_Fa	Mon_Sap_Non _Fo_Fa	Pyr_Di_En_Fs	Kao_Ant_Gre (2)_Or_Ab_An_Fa
	Mon_Sap_Non _Fa	Mon_Sap_Non _Fa	Talc_Min_Di_En_Fs	Kao_Ant_Gre (2)_Di_En_Fs
	Mon_Sap_Fa	Mon_Sap_Fa	Talc_Pyr_Di_En_Fs	Kao_Ant_Gre (2)_Di_Fs
	Or_Ab_An_Sap_Non	Or_Ab_An_Sap_Non	Talc_Pyr_Min_Fo_Fa	Kao_Ant_Di_Fs
	Or_Ab_An_Sap_Non_En_Fs	Or_Ab_An_Sap_Non_En_Fs	Talc_Fo_Fa	Kao_Ant_Gre (2)_Di_En
	Or_Ab_An_Sap_Non_En_	Or_Ab_An_Sap_Non_En	Talc_Fa	Kao_Gre_Di_En
	Or_Ab_An_Non_En_	Or_Ab_An_Non_En_	Or_Ab_An_Talc_Pyr	Kao_Ant_Gre (2)_Fo_Fa
	Or_Ab_An_Mon_Sap	Or_Ab_An_Mon_Sap	Or_Ab_An_Talc_Pyr_Fs	Kao_Ant_Gre (2)__Fa
	Or_Ab_An_Mon_Sap_En_Fs	Or_Ab_An_Mon_Sap_En_Fs	***Or_Ab_An_Talc_Pyr_Fa***	Or_Ab_An_Kao_Ant
	Or_Ab_An_Mon_Sap_Fs	*Or_Ab_An_Mon_Sap_Fs*	Or_Ab_An_Talc_Min	**Or_Ab_An_Kao_Ant_Fs**
	Or_Ab_An_Mon_Non	Or_Ab_An_Mon_Non	Or_Ab_An_Talc_Min_En	**Or_Ab_An_Kao_Ant_Fa**
	Or_Ab_An_Mon_Non_En_Fs	Or_Ab_An_Mon_Non_En_Fs	Or_Ab_An_Min_En	Or_Ab_An_Kao_Gre (2)
	Or_Ab_An_Mon_Non_En	Or_Ab_An_Mon_Non_En	Or_Ab_An_Talc_Min_Fo	**Or_Ab_An_Kao_Gre (2)_En**
	Or_Ab_Mon_Non_En	Or_Ab_Mon_Non_En	Or_Ab_An_Min_Fo	**Or_Ab_An_Kao_Gre (3)_En**
	Or_Ab_An_Mon_En_Fs	*Or_Ab_An_Mon_En_Fs*	Or_Ab_An_Pyr_Min	Or_Ab_An_Kao_Gre (2)_Fo
	Or_Ab_An_Sap_Fs	Or_Ab_An_Sap_Fs	*Or_Ab_An_Pyr_En_Fs*	Or_Ab_An_Kao_Gre (3)_Fo
				Or_Ab_An_Ant_Gre (2)
				Or_Ab_An_Kao
				Or_Ab_An_Kao_En_Fs
				Or_Ab_An_Kao_Fo_Fa
				Or_Ab_An_Ant
				Or_Ab_An_Ant_Fs
				Or_Ab_An_Ant_Fa
				Or_Ab_An_Gre (2)
				Or_Ab_An_Gre (2)_En
				Or_Ab_An_Gre (2)_Fo

[a]Font keys: Regular, poor match to both compositions; italic, borderline match to Mastodon composition only; italic bold, good match to both compositions, but having >14 wt% olivine, contradicting with MB data; bold, good match to both compositions.

[b]Or, orthoclase; Ab, albite; An, anorthite; Di, diopside; En, enstatite; Fs, ferrosilite; Fo, forsterite; Fa, fayalite.

[c]Mon, montmorillonite; Sap, saponite; Non, nontronite.

[d]Mon, montmorillonite; Sap, saponite; Non, nontronite.

[e]Pyr, pyrophyllite; Min, minnesotaite.

[f]Kao, kaolinite; Ant, antigorite; Gre (2), greenalite (Fe2+); Gre (3), greenalite (Fe3+).

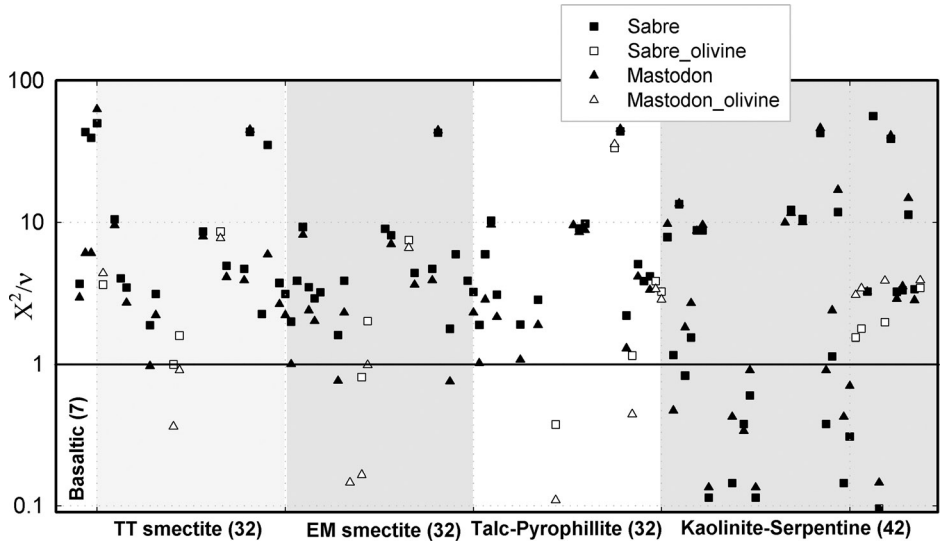

Figure 16. $\chi 2/\nu$ values obtained from 290 mass-balance mixing-model calculations (using 145 sets of mineral assemblages) for the compositions of abraded Sabre and Mastodon of Wooly Patch illustrate the selectivity of the mixing model. The mineral assemblages with $\chi 2/\nu > 100$ and those that contain negative proportions of minerals are not shown. Unfilled symbols are for assemblages containing >14 mass% olivine, which is not allowed by the Mössbauer results.

comprise the 32 mineral sets used in the mixing-model calculations.

[48] With an increasing amount of water and degree of infiltration in the weathering process, the soluble metal cations within smectite minerals could be further leached, forming minerals of the kaolinite group [*Langmuir*, 1997], including nacrite, dickite and halloysite. Kaolinite is the most stable clay mineral under mildly acidic weathering conditions, in which highly soluble alkalis and alkaline-earth elements are readily removed from the host-rock (at high water-to-rock ratio). Serpentine and chlorite minerals have the same ratios of interstitial cations (Mg, Al, Fe) to tetrahedral cations (Si, Al) as kaolinite, and are common alteration products of hydrothermal processes and chemical weathering of the ferromagnesian minerals in igneous rocks. We use kaolinite, antigorite, and greenalite as the three compositional end-members for the kaolinite mineral set, with a chemical formula $[X_{4or6}(Si_4O_{10})(OH)_8]$, where X represents Al, Mg, and Fe. The three end-members actually cover a wide range of phyllosilicates with IC/TC ratio ~4/4 or 6/4, such as all kaolinite, all serpentines, all chlorites, and all septechlorites including chamosite, amesite, and cronstedtite. Combinations of these hydrated minerals and anhydrous basaltic minerals comprise 42 mineral sets used for mixing-model analysis.

[49] Amorphous SiO_2 and amorphous silicates with a medium degree of polymerization [*Kuebler et al.*, 2004; *Tosca et al.*, 2004] are observed in alteration products of various chemical-weathering processes involving common minerals of terrestrial igneous rocks. We use SiO_2 to represent them in the mixing model (Table 5). Allophane-type amorphous phases are observed in terrestrial alteration, and their compositions $[Al_2O_3 \cdot (SiO_2)_{1.3\text{-}2} \cdot (H_2O)_{2.5\text{-}3}]$ can be represented by the combinations of kaolinite and amorphous SiO_2 in the mixing models.

3.3.3. Results of Mixing-Model Calculations

[50] As a test of the mixing-model approach, we first applied it to the composition of abraded Adirondack, a well-studied plains basalt [*McSween et al.*, 2004, 2006]. We started with the compositional end-members of the major basaltic minerals, olivine, pyroxenes, and feldspar, along with accessory minerals phosphate, ilmenite, chromite, and magnetite. The least-squares solution yielded almost identical mineral proportions as those determined with the normative mineralogy calculation (Table 4). For the mineral compositions of plagioclase, pyroxene, and olivine, the mixing model obtained An_{50}, En_{44}, and Fo_{45}, compared to An_{51}, En_{47}, Fo_{47} from the normative calculation. The ratios of MgFe-olivine/(MgFe-pyroxene + MgFe-olivine) from the two calculations are in the range of 0.60–0.61, which match very well with the ~0.61 value of Fe-olivine/(Fe-olivine + Fe-pyroxene) determined by Mössbauer spectral analysis [*Morris et al.*, 2004]. There was no improvement to the model fit by adding any phyllosilicates to the mixture.

[51] For the mass-balance mixing-model analyses for the compositions of abraded Sabre and abraded Mastodon, we used 145 mineral assemblages of basaltic and phyllosilicate minerals described in the previous section as inputs (Table 5). In the following discussion, we define a "good fit" as a model (set of minerals) that provides a value of χ^2/ν of < 1, a "poor fit" as those for which $\chi^2/\nu \gg 1$, and set $1 < \chi^2/\nu < 1.5$ as the dividing zone for the convenience of comparison. For both abraded Sabre and Mastodon, none of the seven basaltic mineral sets tested can account for the rock compositions, as shown in the "basaltic" field of Figure 16 by the high χ^2/ν values. These results are consistent with conclusions drawn from the normative mineralogy calculations (Table 4).

[52] When including phyllosilicates of the smectite group or talc-pyrophyllite (dehydrated smectite) group in the

Table 6. Proportions of Mineral Classes Obtained From One of the Mass-Balance Mixing-Model Calculations

Rock target	Adirondack-RAT		Wooly Patch-Mastodon		Wooly Patch-Sabre			
							Average of ten results calculated using ten sets of generated compositions based on normal cumulated distribution	
Mixing model calculation	Table 2 composition		Table 2 composition		Table 2 composition			
Mineral classes	Mass%	±[a]	Mass%	±[a]	Mass%	±[a]	Mass%	Std[b]
Chlorite	0.3	0.0	1.7	0.1	1.3	0.1	1.4	0.2
Sulfate	1.9	0.0	4.0	0.2	4.7	0.2	4.7	0.6
Phosphate	1.2	0.0	2.7	0.0	2.7	0.0	3.3	0.6
Fe-oxides and hydroxides	5.0	0.1	7.8	0.2	7.4	0.2	6.7	0.3
Feldspar	38.9	0.2	22.3	1.9	25.5	1.6	27.4	4.7
Pyroxene	31.2	0.7	47.8	1.3	41.0	1.1	40.3	2.6
Olivine	21.5	0.6						
Kaolinite-serpentine			13.7	1.2	17.4	1.1	16.2	3.7
Total	100		100		100		100	

[a]Standard deviation of mixing model.
[b]Standard deviation over ten calculated results.

mineral assemblages (total of 192 sets for Mastodon and Sabre), 91% of them cannot account for the two rock compositions as shown in the fields of ''TT smectite,'' ''EM smectite,'' and ''Talc - pyrophyllite'' of Figure 16. All mineral sets providing good fits require 14–20 mass% of olivine (forsterite, fayalite or some mixture thereof, shown in Figure 16 as unfilled symbols below the line of $\chi^2/\nu = 1$ in the three fields given above). This result contradicts the Mössbauer results for Wooly Patch, which indicate that only 2–3 mass% of the Fe can be assigned as $Fe^{2+}_{olivine}$ (Table 3), even if there is a similar or slightly higher amount of Mg-olivine. The remaining mineral sets (4% of total sets tested) provide borderline fits to the Mastodon composition only (filled triangles near $\chi^2/\nu \sim 1$ line in Figure 16). Thus we conclude that smectites or talc-pyrophyllites are not the likely hosts of the excess of Al_2O_3 and SiO_2 in Wooly Patch.

[53] When adding phyllosilicates of the kaolinite-serpentine group into the mineral assemblages (total of 84 sets for Mastodon and Sabre), 20 of the 84 mineral sets tested provide good or borderline fit to both Sabre and Mastodon compositions. Those mineral sets that account best for Wooly Patch compositions are combinations of end-members of the kaolinite (kaolinite, antigorite, and greenalite), feldspar (orthoclase, albite, and anorthite), and pyroxene (enstatite, ferrosilite, diopside) groups (mineral assemblages in bold text of Table 5). Thus we conclude that Wooly Patch likely contains phyllosilicates such as kaolinite, antigorite, and greenalite.

[54] For the best-fit solutions, the mass-balance model does not provide a strong constraint on the ratio of Ca-pyroxene to anorthite, that is, one could be less and the other more than for the ''best-fit'' by a few percent while still providing a ''good fit.'' Similarly, the model does not strongly constrain the ratio of the Mg end-members of the kaolinite group and the pyroxene group (i.e., replacing antigorite by enstatite, or vice versa), or Fe end-members (replacing greenalite by ferrosilite, or vice versa). Moreover, the valence state of Fe in greenalite does not have a big effect on the goodness of fit (Table 5, variations in $\chi^2/\nu < 0.3$). When introducing SiO_2 into any of these twenty mineral assemblages that provide good fits, the goodness of fit is always improved by a factor of 2 to 5. In contrast, poor fits are obtained when using olivine to replace the Mg- and Fe-end-members of pyroxene (i.e., replace enstatite by forsterite, or replace ferrosilite by fayalite) or kaolinite-serpentine group (replace antigorite by forsterite, or replace greenalite by fayalite) within the assemblages (the un-filled symbols in ''kaolinite-serpentine'' field of Figure 16). This result is consistent with the Mössbauer spectroscopic observation (paucity of $Fe^{2+}_{olivine}$) and the current understanding of dissolution rates of basaltic minerals (olivine > glass > plagioclase > clinopyroxene > Fe-Ti-oxides) in acidic weathering environments [*Nesbitt and Wilson*, 1992].

[55] Abraded Sabre and abraded Mastodon differ compositionally from each other and the differences are quantitatively represented by different relative proportions of mineral phases. The model suggests that abraded Sabre contains 17 mass% phyllosilicates while abraded Mastodon contains 14 mass% (Table 6). The Sabre target is probably more altered because it was selected near a surface fracture whereas the Mastodon target is in an area away from edges and fractures, and possibly holds the most representative chemistry for the interior of Wooly Patch.

3.3.4. Direct Interpretation and Extrapolation of Mixing Model Results

[56] A first-order and unambiguous result of the mass-balance analysis is that it identifies the type of mineral assemblages that cannot account for the measured composition. Mineral assemblages that do not account for the composition of the Wooly Patch outcrop (discounting oxides and salts) are basaltic mineral mixtures, mixtures of smectite minerals and basaltic minerals, and mixtures of talc - pyrophyllite - minnesotaite minerals (or dehydrated smectites) with basaltic minerals.

[57] The mass-balance analysis also indicates what mineral assemblages can account for the measured compositions. For the Wooly Patch outcrop, 20 of the mineral sets tested can account for the measured compositions. All contain kaolinite-serpentine groups of phyllosilicates, plus varieties of feldspars and pyroxenes. The flexibility in mineral combinations within a similar type of mineral assemblage (kaolinite-serpentine plus basaltic) reflects both the selectivity and robustness of the mixing model, which will be discussed below. It is necessary, however, to have some other direct mineralogical detection to demonstrate

Table 7. Ratio of Total Interstitial Cations to Tetrahedral Cations for Major Classes of Silicates[a]

Silicate Class, Typical Minerals	NBO	Chemical Formula	Cation Ratios	
			IC_T/TC	Ratio
Ortho-silicate				
Garnet	4	$(Mg, Fe, Ca)_3Al_2Si_3O_{12}$	5/3	1.67
Olivine	4	$(Mg, Fe)_2SiO_4$	2/1	2
Soro- and cyclo-silicate				
Epidote	3	$Ca_2(Al, Fe)_3Si_3O_{12}(OH)$	5/3	1.7
Beryl -cordierite	2	$(Be, Al)_3(Al, Mg)_2(Si, Al)_6O_{18}$	5/6	0.83
Chain-silicate				
Pyroxene	2	$(Mg, Fe)_2Si_2O_6$	2/2	1
Ca-pyroxene	2	$Ca\ (Mg, Fe)Si_2O_6$	2/2	1
Pyroxenoid	2	$(Ca, Mn, Fe)_3Si_3O_9$	3/3	1
Amphibole	1.5	$(Mg, Fe)_7Si_8O_{22}(OH)_2$	7/8	0.88

Silicate Class, Typical Minerals	NBO	Chemical Formula	Cation Ratios		
			IC_T/TC	Trioct	Dioct
Phyllo-silicates					
Smectite group					
Montmorillonite	1	$Ca_{0.33}(Mg_{0.66}\ Al_{3.34})Si_8O_{20}(OH)_4$	4.33/8		0.54
Nontronite	1	$(Ca_{0.33})Fe_4(Si_{7.34}\ Al_{0.66})O_{20}(OH)_4$	4.33/8		0.54
Saponite	1	$Na_{0.66}\ Mg_6(Si_{7.34}\ Al_{0.66})O_{20}(OH)_4$	6.7/8	0.84	
Vermiculite	1	$(Mg, Ca)_{0.7}(Mg, Fe^{3+}, Al)_6[(Si, Al)_8O_{20}](OH)_4.8H_2O$	6.7/8	0.84	
Talc group					
Pyrophyllite	1	$Al_2(Si_4O_{10})(OH)_2$	2/4		0.5
Talc-minnesotaite	1	$(Mg, Fe)_3(Si_4O_{10})(OH)_2$	3/4	0.75	
Kaolinite group					
Kaolinite	1	$Al_4(Si_4O_{10})(OH)_8$	4/4		1
Serpentine group					
Antigorite-chrysotile–lizardite	1	$(Mg, Fe)_6[(Si, Al)_4O_{10}](OH)_8$	6/4	1.5	
Chlorite group					
Chlorite	1	$(Mg, Fe, Al)_6[(Si, Al)_4O_{10}](OH)_8$	6/4	1.5	
Septechlorite group					
Amesite	1	$(Mg_4Al_2)(Si_2Al_2O_{10})(OH)_8$	6/4	1.5	
Chamosite	1	$(Fe^{2+}Al_2)(Si_2Al_2O_{10})(OH)_8$	6/4	1.5	
Greenalite (2)	1	$Fe^{2+}{}_6(SI_4O_{10})(OH)_8$	6/4	1.5	
Cronstedtite	1	$(Fe^{2+}{}_4Fe^{3+}{}_2)(Si_2Fe^{3+}{}_2O_{10})(OH)_8$	6/4	1.5	
Mica group					
Muscovite-paragonite	1	$(K, Na)Al_2[AlSi_3O_{10}](OH)_2$	3/4		0.75
Phlogopite-biotite	1	$K_2(Mg, Fe)_6[Si_6Al_2O_{20}](OH)_4$	8/8	1	
Mica-like group					
Illite	1	$KAl_4[Si, Al)_8O_{20}](OH)_4$	5/8		0.63
Glauconite	1	$(K, Na, Ca)_{1.5}(Fe, Al, Mg)_4[(Si, Al)_8O_{20}(OH)_4.nH_2O$	5.5/8		0.69
Lepidolite	1	$K_2(Li, Al)_{5\text{-}6}[(Si, Al)_8O_{20}(OH)_4$	~8/8	1	
Margarite	1	$Ca_2Al_4[Si_4Al_4O_{20}](OH)_4$	6/8		0.75

Silicate Class, Typical Minerals	NBO	Chemical Formula	Cation Ratios	
			IC_T/TC	Ratio
Tecto-silicate				
Feldspar	0	$(K, Na, Ca)(Si, Al)_4O_8$	1/4	0.25
Zeolite (Thomsonite)	0	$NaCa_2Al_5Si_5O_{20}.6H_2O$	3/10	0–0.3

[a]NBO, nonbridging oxygen; IC_T, total interstitial cations; TC, tetrahedral cations; Trioct, trioctahedral phyllosilicate; Dioct, dioctahedral phyllosilicate.

that these minerals are actually present. Moreover, the resulting models suggest a much wider range of minerals that could be candidates for occurrence in the Wooly Patch outcrop, as shown in Table 7, which lists the IC_T/TC ratios for major types of silicates.

[58] The most important information gained from the mixing model analysis is the type of phyllosilicate, in a broad sense, that matches the cation ratios in the measured compositions. The consistent IC_T/TC ratio (Table 7) for the kaolinite-antigorite-greenalite group matches the compositions of Wooly Patch: ~1.5 for trioctahedral phases and ~1.0 for dioctahedral phases. The mineral groups that have similar IC_T/TC ratios are kaolinite, serpentine, chlorite and septechlorite (Table 7). Therefore the mass-balance mixing-model calculation suggests that these types of phyllosilicates (plus remnants of basaltic minerals) are all good candidates to make up the observed compositions in Wooly Patch.

[59] Data in Table 7 also reveal why certain mineral groups provide a poor fit, and can predict the outcome for untested groups. Within the class of phyllosilicates, smectite- and talc-group minerals have much lower IC_T/TC ratios (0.75–0.84 for trioctahedral phases and ~0.5 for dioctahedral phases, Table 7) than the kaolinite group. Thus a mineral set containing these phyllosilicates would need to have orthosilicates (such as olivine, $IC_T/TC = 2$) in considerable relative abundance (14–20 mass% in our mixing calculations) in order to make up the IC_T/TC ratios in the compositions of Wooly Patch. As noted, however, this type of solution is not allowed by the Mössbauer analysis.

[60] Another major phyllosilicate group is mica and mica-like minerals. Such phases also have low IC_T/TC cation

ratios (1.0 for trioctahedral phases and 0.625–0.75 for dioctahedral phases, Table 7), that would require a reduction of feldspar and an increase of high IC_T/TC type silicates, like olivine, in order to have a "good fit" with Wooly Patch compositions. In addition, micas have not been proposed to be present on the surface of Mars, and have yet to be observed in Martian meteorites. Zeolites have been suggested to be present on Mars [e.g., *Bish et al.*, 2003; *Ruff*, 2004]; however, owing to the lack of small interstitial cations like Mg and Fe in the zeolite structure and their extremely low IC_T/TC cation ratios (0–0.3), we infer that a mineral set containing zeolites would need to have an even higher proportion of orthosilicates (e.g., olivine) in order to match the compositions of Wooly Patch. In addition, Wooly Patch has the lowest Ca and K concentration among all Gusev rocks, which is not indicative of zeolite group minerals that need high amounts of charge-balancing cations such as Ca and K.

[61] We have used stoichiometric crystalline mineral phases as the input for mixing model calculations. As a result, the assemblages proving the good matches contain only the stoichiometric crystalline minerals. Thus our results do not exclude the possibility that some nonstoichiometric or amorphous phases could be part of the Wooly Patch mineral assemblages. For example, some kaolinite-SiO_2-bearing mineral sets that provided good fits suggest the potential existence of allophane-like materials.

3.3.5. Robustness of Mineralogical Assignments Versus Analytical Uncertainties

[62] As a test of the robustness of our mass-balance results with respect to analytical uncertainty, we repeated the modeling exercise on ten test compositions. These compositions have the property that the mean concentration for each element is normally distributed about the concentration value of abraded Sabre (Table 2) with a standard deviation approximating the uncertainty values of Table 1 of *Gellert et al.* [2004] converted to mass% or, as described above, 20% of the mean concentration value for Na.

[63] We ran the mass-balance mixing-model calculations for the ten test compositions using the mineral set that gave the best fit to the original Sabre composition (Table 2). This mineral set contains kaolinite, orthoclase, albite, diopside, enstatite, and ferrosilite plus the minor phases chlorite, sulfates, Ca-phosphate and Fe-oxides. On average, the proportion of each mineral predicted by the mass-balance model for the ten test compositions is the same as that obtained on the observed composition (Table 6). The mean ± standard deviation for the kaolinite component is 16 ± 4 mass%.

4. Conclusion and Implications

[64] The rock known as Wooly Patch is the silicate-rich end-member of Clovis class rocks at West Spur, Columbia Hills. It has distinct characteristics from other Gusev rocks investigated by the full set of Athena science instruments on the Spirit rover. Wooly Patch is the softest rock abraded by the Rock Abrasion Tool at the Gusev landing site (through sol 291). It has a surface morphology suggesting the presence of hardened material at the fracture edges, potentially involving the cementation/deposition of mineral materials from fluid. It shows cataclastic micromorphology in the interior matrix and extremely fine porous cuttings. It has a distinct Vis-NIR spectrum suggesting minerals with strong Fe absorptions in the abraded rock interior. From the Mössbauer spectra, there is a virtual absence of $Fe^{2+}_{olivine}$ and an intense spectral doublet suggesting octahedrally sited Fe^{2+} with somewhat larger quadrupole splitting from the $Fe^{2+}_{pyroxene}$ component within plains basalts. Among rocks for which elemental concentrations were determined by the Alpha-Particle X-ray Spectrometer, Wooly Patch is at the extreme end of the range for several elements (the lowest Ca and K; the highest Al and Ti). Ratios of major silicate-related cations suggest a medium degree of polymerization (e.g., phyllosilicates). The composition has an excess, compared to any basaltic assemblage of minerals, of Al_2O_3 and SiO_2. Mass-balance calculations suggest that the presence of phyllosilicates in this rock can quantitatively account for the excess Al_2O_3 and SiO_2. Those phyllosilicates that account for the composition best are those of the kaolinite, serpentine, chlorite, and septechlorite groups.

[65] Among the weathering products of igneous rocks, kaolinite (including nacrite, dickite, and halloysite) marks the high end of the "intensity of chemical weathering," as measured by the Chemical Index of Alteration (CIA) [*Nesbitt and Wilson*, 1992], and is the most stable weathering product under mildly acidic conditions (i.e., pH 4–6). The pH level and drainage conditions are two factors that control the formation of Al-rich phyllosilicates [*Langmuir*, 1997]. Poor drainage conditions normally allow higher pH levels, because the cations leaching out from primary igneous minerals consume the available acidity to a greater extent when the fluid is more stagnant. Phyllosilicates in the smectite family (montmorillonite, saponite and nontronite) would normally form as primary weathering products of basaltic rocks under these poor drainage, high-pH conditions. When drainage is high enough to flush away the cations and anions produced during the chemical weathering reactions of basalt, the pH level of the fluid can be kept somewhat lower. This slightly more acidic fluid would continue to react with the remaining cations in basaltic mineral phases, and would react with the cations (Ca, Mg, Fe, Na, K) incorporated into secondary weathering products, such as smectite, illite, or vermiculite, possibly removing them from the vicinity after dissolution. As a result, the most insoluble component of these minerals, Al, will be left; kaolinite-type phyllosilicates would form and remain. Further alteration, with acidity increase, would destroy kaolinite-type minerals, and Al- and Fe-oxides/hydroxides would be the end products [*Langmuir*, 1997].

[66] This scenario may have very important implications for the formation of Wooly Patch. Wooly Patch is highly depleted in Ca (the lowest among all Gusev rock hitherto), enriched in Al, and especially enriched in Ti. Ti typically resides in FeTi-oxides, which are last to be dissolved in acidic weathering processes [*Nesbitt and Wilson*, 1992]. The compositional features of Wooly Patch and the results of mixing model analysis could be a good indication of a leaching process, which led to the formation of Al-rich phyllosilicates.

[67] The kaolinite group of phyllosilicates can form from the chemical weathering of feldspar and feldspathoid minerals in plutonic and volcanic rocks. These minerals can also form from the glassy materials within volcanic ash.

Pyroclastic materials have been suggested as a likely precursor of West Spur rocks by textural observations in the rock interior of this area [*Arvidson et al.*, 2006]. Basaltic glass was one of the major components from the Mini-TES spectral deconvolution of a nearby rock (Pico, found near Clovis) at West Spur [*Ruff et al.*, 2005]. Relative to the primary basaltic minerals, basaltic glass has the second fastest dissolution rate (only less than olivine) as observed in terrestrial rocks [*Nesbitt and Wilson*, 1992]. Basaltic glass may have also been a significant source of Al to solution [*Tosca et al.*, 2004], possibly facilitating the production of phyllosilicates under suitable pH conditions. Studies by *Gooding and Keil* [1978] using thermodynamic calculations indicated that under the present Martian conditions, the derivation of metastable clay minerals by chemical weathering appears to be more favorable when silicate glasses, rather than mineral crystals, are the primary phases being altered. Normally, natural glasses may alter either by devitrification (crystallization) or chemical weathering (decomposition into new and chemically distinct phases). A selection among the two potential pathways would be determined by the greatest negative Gibbs free energy changes under specific conditions [*Gooding and Keil*, 1978]: high temperature and inert environments would favor devitrification; low temperature and reactive environments (such as Gusev) would favor chemical decomposition. For each compositional case that *Gooding and Keil* [1978] calculated, a decrease of temperature would enlarge the stability field of minerals such as kaolinite and beidellite.

[68] Amorphous silica with a higher degree of polymerization than chain silicates occurs as a chemical weathering product of both terrestrial and synthetic olivine [*Kuebler et al.*, 2004; *Tosca et al.*, 2004]. An excess of SiO_2 (as well as Al_2O_3) is implied in Wooly Patch by normative mineral calculations. In mixing-model analyses, adding SiO_2 as a component would significantly improve the compositional matches, although it is not a necessary condition to making the kaolinite-bearing assemblage satisfy a goodness of fit criterion (e.g., to make $\chi^2/\nu < 1$). Nevertheless a good match of kaolinite-SiO_2-bearing mineral sets to Wooly Patch compositions may also be indicative of allophane-like amorphous materials $[Al_2O_3{\cdot}(SiO_2)_{1.3\text{-}2}{\cdot}(H_2O)_{2.5\text{-}3}]$. If acidic alteration did occur in Wooly Patch, amorphous silica could have been formed as a residual phase left over from alteration of primary igneous materials, which would coexist with kaolinite-type phyllosilicates and anatase (TiO_2) as observed in many terrestrial deposits [*Langmuir*, 1997].

[69] The antigorite and greenalite end-members in the tested mineral assemblages are meant to account for the Mg and Fe portions of a phyllosilicate composition, which would match the Wooly Patch rock composition when combined with some remnants of primary basaltic materials. It is necessary to do so because kaolinite is a relatively pure mineral (unlike other clay minerals), and its bulk composition does not vary appreciably. IC_T/TC cation ratio comparison has widened the range of phyllosilicates that can account for the Wooly Patch compositions, i.e., to include serpentine, chlorite, and septechlorite. These types of minerals, however, would form under very specific conditions, such as hydrothermal alteration of ultrabasic rocks, and there is not sufficient evidence yet to suggest this type of process occurred in the West Spur rocks. One positive observation that might support the hypothesis of serpentinization of olivine and pyroxene would be the definitive identification of secondary magnetite (C. Schröder, Evidence for olivine weathering in rocks at Gusev crater, manuscript in preparation, 2006). To find more direct analytical evidence for definitive identification of Mg- and Fe-phases is important. A more detailed study on the mineralogical assignment of the spectral doublet associated with the octahedral Fe^{2+} in the Mössbauer spectra of Wooly Patch would help to constrain the problem. At present, the serpentine or chlorite types of phyllosilicates cannot be excluded because they have the right type of IC_T/TC ratio to match the Wooly Patch compositions.

[70] The potential existence of kaolinite-type phyllosilicates within Wooly Patch (and possibly in other West Spur rocks) suggests a mildly (pH 4–6) acidic environment in the past, and an open hydrologic system with adequate drainage conditions to facilitate their production.

[71] **Acknowledgments.** We thank the NASA Mars program for supporting our participation in the Mars Exploration Rover mission. We thank the JPL management and the engineering teams for their innovative and dedicated handling of the rovers; both of the rovers are still in good health as of this writing and are continuing the exploration of Mars. One of the coauthors, Larry A. Haskin, passed away on 24 March 2005 during the preparation of this manuscript. Larry provided major support and guidance during the development of the analyses for the silicate mineralogy of Wooly Patch. Larry Haskin will be remembered by the coauthors and by the Athena science team for his dedication from the start of the Athena Science Instrument Payload, for his leadership in developing the Athena Microbeam Raman Spectrometer, and for his contributions during the Mars Exploration Rover mission. We are also thankful to S. McLennan, R. Gellert, R. Morris, and D. Ming for their instructive suggestions and comments. We thank the two reviewers, Leslie L. Baker and Michelle Minitti. Their instructive comments and suggestions helped us to strengthen this paper.

References

Arvidson, R. E., F. Poulet, J.-P. Bibring, M. Wolff, A. Gendrin, R. C. Morris, J. J. Freeman, Y. Langevin, N. Mangold, and G. Bellucci (2005), Spectral reflectance and morphologic correlations in eastern Terra Meridiani, Mars, *Science*, *307*, 591–1593, doi:10.1126/science.1109509.

Arvidson, R. V., et al. (2006), Overview of the Spirit Mars Exploration Rover Mission to Gusev Crater: Landing site to Backstay Rock in the Columbia Hills, *J. Geophys. Res.*, *111*, E02S01, doi:10.1029/2005JE002499.

Bartlett, P. W., L. E. Carlson, P. C. Chu, K. R. Davis, S. P. Gorevan, A. G. Kusack, T. M. Myrick, J. J. Wilson, and the Athena Science Team (2005), Summary of Rock Abrasion Tool (RAT) results pertinent to the Mars Exploration Rover science data set, *Lunar Planet. Sci.*, *XXXVI*, abstract 2292.

Bell, J. F., III, et al. (2003), Mars Exploration Rover Athena Panoramic Camera (Pancam) investigation, *J. Geophys. Res.*, *108*(E12), 8063, doi:10.1029/2003JE002070.

Bell, J. F., III, et al. (2004), Pancam multispectral imaging results from the Spirit rover at Gusev Crater, *Science*, *305*, 800–806.

Bibring, J.-P., et al. (2005), Mars surface diversity as observed by the OMEGA/Mars Express investigation, *Science*, *307*, 1576–1581, doi:10.1126/science.1108806.

Bish, D. L., J. W. Carey, D. T. Vaniman, and S. J. Chipera (2003), Stability of hydrous minerals on the Martian surface, *Icarus*, *164*, 96–103, doi:10.1016/s0019-1035(03)00140-4.

Blum, A., and L. Stilling (1995), Feldspar dissolution kinetics, in *Chemical Weathering Rates of Silicate Minerals*, edited by A. White and S. Brantley, pp. 291–352, Mineral. Soc. of Am., Washington, D. C.

Brain, D. C., and J. D. Russell (1980), Swelling minerals in a basalt and its weathering products from Mover, Scotland: I. Interstratified montmorillonite-vermiculite-illite, *Clay Miner.*, *15*, 445–451.

Burbine, T. H., and K. M. O'Brien (2004), Determining the possible building blocks of the Earth and Mars, *Meteorit. Planet. Sci.*, *39*, 667–681.

Burns, R. G., and D. S. Fisher (1990), Iron-sulfur mineralogy of Mars: Magmatic evolution and chemical weathering products, *J. Geophys. Res.*, *95*, 14,415–14,421.

Christensen, P. R., et al. (2003), Miniature Thermal Emission Spectrometer for the Mars Exploration Rovers, *J. Geophys. Res.*, *108*(E12), 8064, doi:10.1029/2003JE002117.

Christensen, P. R., et al. (2004), Initial results from the Mini-TES experiment in Gusev Crater from the Spirit rover, *Science*, *305*, 837–842.

Craig, D. C., and F. C. Loughnan (1964), Chemical and mineralogical transformations accompanying the weathering of basic volcanic rocks of New South Wales, *Aust. J. Soil Res.*, *2*, 218–234.

Cross, C. W., J. P. Iddings, L. V. Pirsson, and H. S. Washington (1902), A quantitative chemico-mineralogical classification and nomenclature of igneous rocks, *J. Geol.*, *10*, 555–690.

Crumpler, L. S., et al. (2005), Mars Exploration Rover geologic traverse science by the Spirit rover in the plains of Gusev Crater, Mars, *Geology*, *33*(10), 809–812.

Deer, W. A., R. A. Howie, and J. Zussman (1963), *Rock-Forming Minerals*, John Wiley, Hoboken, N. J.

Eichelberger, J. C., and F. G. Koch (1979), Lithic fragments in the Bandelier Tuff, Jemez Mountains, New Mexico, *J. Volcanol. Geotherm. Res.*, *5*, 115–134.

Farrand, W. H., J. F. Bell III, J. R. Johnson, S. W. Squyres, J. Soderblom, and D. W. Ming (2006), Spectral variability among rocks in visible and near-infrared multispectral Pancam data collected at Gusev crater: Examinations using spectral mixture analysis and related techniques, *J. Geophys. Res.*, *111*, E02S15, doi:10.1029/2005JE002495.

Gellert, R., et al. (2004), Chemistry of rocks and soils in Gusev Crater from the Alpha Particle X-Ray Spectrometer, *Science*, *305*, 829–832.

Gellert, R., et al. (2006), Alpha Particle X-Ray Spectrometer (APXS): Results from Gusev crater and calibration report, *J. Geophys. Res.*, *111*, E02S05, doi:10.1029/2005JE002555.

Gendrin, A., et al. (2005), Sulfates in Martian layered terrains: The OMEGA/Mars Express view, *Science*, *307*, 1587–1591, doi:10.1126/science.1109087.

Gooding, J. L. (1992), Soil mineralogy and chemistry on Mars: Possible clues from salts and clays in SNC meteorites, *Icarus*, *99*, 28–41.

Gooding, J. L., and K. Keil (1978), Alteration of glass as a possible source of clay minerals on Mars, *Geophys. Res. Lett.*, *5*, 727–730.

Gorevan, S. P., et al. (2003), Rock Abrasion Tool: Mars Exploration Rover mission, *J. Geophys. Res.*, *108*(E12), 8068, doi:10.1029/2003JE002061.

Görlich, K., E. A. Görlich, K. Tomala, and P. Q. Hung (1989), ^{57}Fe Mössbauer study of a sediment column in the Gdansk Basin, Baltic Sea: Palaeoenvironmental application, *Mar. Geol.*, *88*(1–2), 49–69.

Grandstaff, D. E. (1977), Some kinetics of bronzite orthopyroxene dissolution, *Geochim. Cosmochim. Acta*, *41*, 1097–1103.

Greeley, R., et al. (2004), Wind-related processes detected by the Spirit rover at Gusev Crater, Mars, *Science*, *305*, 810–821.

Gunter, A. E., G. B. Skippen, and G. Y. Chao (1984), Cell dimensions, Mössbauer and infrared absorption spectra of synthetic cordierite, *Can. Mineral.*, *22*, 447–452.

Haskin, L. A., et al. (2005), Water alteration of rocks and soils from the Spirit rover site, Gusev Crater, Mars, *Nature*, *436*, 66–69.

Herkenhoff, K. E., et al. (2003), Athena Microscopic Imager investigation, *J. Geophys. Res.*, *108*(E12), 8065, doi:10.1029/2003JE002076.

Huguenin, R. L. (1974), The formation of goethite and hydrated clay minerals on Mars, *J. Geophys. Res.*, *79*, 3895–3905.

Klingelhöfer, G., et al. (2003), Athena MIMOS II Mössbauer spectrometer investigation, *J. Geophys. Res.*, *108*(E12), 8067, doi:10.1029/2003JE002138.

Knauss, K. G., S. N. Nguyen, and H. C. Weed (1993), Diopside dissolution kinetics as a function of pH, CO_2, temperature, and time, *Geochim. Cosmochim. Acta*, *57*, 285–294.

Korotev, R. L. (1997), Some things we can infer about the Moon from the composition of the Apollo 16 regolith, *Meteorit. Planet. Sci.*, *32*, 447–478.

Korotev, R. L., and D. T. Kremser (1992), Compositional variations in Apollo 17 soils and their relationship to the geology of the Taurus-Littrow site, *Proc. Lunar Planet. Sci. Conf. 22nd*, 275–301.

Korotev, R. L., L. A. Haskin, and B. L. Jolliff (1995), A simulated geochemical rover mission to the Taurus Littrow valley of the Moon, *J. Geophys. Res.*, *100*, 14,403–14,420.

Kuebler, K., A. Wang, B. L. Jolliff, and L. A. Haskin (2004), A survey of olivine alteration products using Raman spectroscopy, *Proc. Lunar Planet. Sci. Conf. 35th*, Abstract 1704.

Langmuir, D. (1997), *Aqueous Environmental Heochemistry*, 600 pp., Prentice-Hall, Upper Saddle River, N. J.

Larsen, K., R. E. Arvidson, B. L. Jolliff, and B. E. Clark (2000), Correspondence and least squares analyses of soil and rock compositions for the Viking Lander 1 and Pathfinder landing sites, *J. Geophys. Res.*, *105*, 29,207–29,221.

Li, R., et al. (2006), Spirit rover localization and topographic mapping at the landing site of Gusev crater, Mars, *J. Geophys. Res.*, *111*, E02S06, doi:10.1029/2005JE002483.

Matsui, Y., Y. Syono, and Y. Maeda (1972), Mössbauer spectra of synthetic and natural calcium rich clinopyroxenes, *Mineral. J.*, *7*, 88–107.

McSween, H. Y. (2005), Chemical composition of unconsolidated sediments on Mars, *Geol. Soc. Am. Abstr. Programs*, *37*(7), 546.

McSween, H. Y., et al. (2004), Basaltic rocks analyzed by the Spirit rover in Gusev Crater, *Science*, *305*, 842–845.

McSween, H. Y., et al. (2006), Characterization and petrologic interpretation of olivine-rich basalts at Gusev Crater, Mars, *J. Geophys. Res.*, *111*, E02S10, doi:10.1029/2005JE002477.

Ming, D. W., et al. (2006), Geochemical and mineralogical indicators for aqueous processes in the Columbia Hills of Gusev crater, Mars, *J. Geophys. Res.*, *111*, E02S12, doi:10.1029/2005JE002560.

Morris, R. V., et al. (2004), Mineralogy at Gusev Crater from the Mössbauer Spectrometer on the Spirit rover, *Science*, *305*, 833–836.

Morris, R. V., D. W. Ming, B. C. Clark, G. Klingelhoefer, R. Gellert, D. Rodionov, C. Schroeder, P. de Souza, A. Yen, and the Athena Science Team (2005), Abundance and speciation of water and sulfate at Gusev Crater and Meridiani Planum, *Lunar Planet. Sci.*, *XXXVI*, Abstract 2239.

Morris, R. V., et al. (2006), Mössbauer mineralogy of rock, soil, and dust at Gusev crater, Mars: Spirit's journey through weakly altered olivine basalt on the Plains and pervasively altered basalt in the Columbia Hills, *J. Geophys. Res.*, doi:10.1029/2005JE002584, in press.

Nesbitt, H. W., and R. E. Wilson (1992), Recent chemical weathering of basalts, *Am. J. Sci.*, *292*, 740–777.

Nesbitt, H. W., and G. M. Young (1984), Prediction of some weathering trends of plutonic and volcanic rocks based on thermodynamic and kinetic considerations, *Geochim. Cosmochim. Acta*, *48*, 1523–1534.

Pokrovsky, O., and J. Schott (2000a), Forsterite surface composition in aqueous solutions: A combined potentiometric, electrokinetic, and spectroscopic approach, *Geochim. Cosmochim. Acta*, *64*, 3299–3312.

Pokrovsky, O., and J. Schott (2000b), Kinetics and mechanism of forsterite dissolution at 25C and pH from 1 to 12, *Geochim. Cosmochim. Acta*, *64*, 3313–3325.

Rieder, R., R. Gellert, J. Brückner, G. Klingelhöfer, G. Dreibus, A. Yen, and S. W. Squyres (2003), The new Athena alpha particle X-ray spectrometer for the Mars Exploration Rovers, *J. Geophys. Res.*, *108*(E12), 8066, doi:10.1029/2003JE002150.

Robinson, D. A., and R. B. G. Williams (1995), *Rock Weathering and Landform Evolution*, 544 pp., John Wiley, Hoboken, N. J.

Ruff, S. W. (2004), Spectral evidence for zeolite in the dust on Mars, *Icarus*, *168*, 131–143.

Ruff, S. W., P. R. Christensen, and the Athena Science Team (2005), The rocks of Gusev crater as viewed by MiniTES, *Lunar Planet. Sci.*, *XXXVI*, abstract 2155.

Schott, J., R. A. Berner, and E. L. Sjoberg (1981), Mechanism of pyroxene and amphibole weathering—I. Experimental studies of iron-free minerals, *Geochim. Cosmochim. Acta*, *45*, 2123–2135.

Smith, R. L., and R. A. Bailey (1966), The Bandelier tuff, a study of ash-flow eruption cycles from zoned magma chambers, *Bull. Volcanol.*, *29*, 83–104.

Squyres, S. W., et al. (2003), Athena Mars rover science investigation, *J. Geophys. Res.*, *108*(E12), 8062, doi:10.1029/2003JE002121.

Squyres, S. W., et al. (2004), The Spirit Rover's Athena science investigation at Gusev Crater, Mars, *Science*, *305*, 794–799.

Squyres, S. W., et al. (2006), Rocks of the Columbia Hills, *J. Geophys. Res.*, *111*, E02S11, doi:10.1029/2005JE002562.

Tosca, N. J., S. M. McLennan, D. H. Lindsley, and M. A. A. Schoonen (2004), Acid-sulfate weathering of synthetic Martian basalt: The acid fog model revisited, *J. Geophys. Res.*, *109*, E05003, doi:10.1029/2003JE002218.

Wang, A., L. A. Haskin, R. L. Korotev, B. L. Jolliff, P. de Souza Jr., A. G. Kusack, and the Athena Science Team (2005a), Evidence of phyllosilicate in Wooly Patch—An altered rock encountered on the Spirit rover traverse, *Lunar Planet Sci.*, *XXXVI*, Abstract 2327.

Wang, A., et al. (2005b), Sulfate deposition in regolith exposed in trenches on the plains between the Spirit landing site and Columbia Hills in Gusev Crater, Mars, *Lunar Planet. Sci.*, *XXXVI*, Abstract 2236.

Wang, A., et al. (2006), Sulfate deposition in subsurface regolith in Gusev crater, Mars, *J. Geophys. Res.*, doi:10.1029/2005JE002513, in press.

Wogelius, R., and J. Walther (1992), Olivine dissolution kinetics at near-surface conditions, *Chem. Geol.*, *97*, 101–112.

L. Crumpler, New Mexico Museum of Natural History and Science, 1801 Mountain Road, Albuquerque, NM 87104, USA.

P. de Souza Jr., Companhia Vale do Rio Doce, Rio de Janeiro, RJ, Brazil.

W. H. Farrand, Space Science Institute, 4750 Walnut Street, Boulder, CO 80301, USA.

K. E. Herkenhoff, U.S. Geological Survey, 2255 North Gemini Drive, Flagstaff, AZ 86001, USA.

J. A. Hurowitz and N. J. Tosca, Department of Geosciences, State University of New York, Stony Brook, NY 11794-2100, USA.

B. L. Jolliff, R. L. Korotev, and A. Wang, Department of Earth and Planetary Sciences, Washington University, Campus Box 1169, One Brookings Drive, St. Louis, MO 63130, USA. (alianw@levee.wustl.edu)

A. G. Kusack, Honeybee Robotics, 460 West 34th Street, New York, NY 10001, USA.